ppGpp Coordinates Nucleotide and Amino-Acid Synthesis in E. coli During Starvation

Citation: Boyuan Wang, Robert A. Grant, Michael T. Laub, ppGpp Coordinates Nucleotide and Amino-Acid Synthesis in E. coli During Starvation, Molecular Cell, Volume 80, Issue 1, 2020 © 2020 Elsevier Inc.

As Published: 10.1016/J.MOLCEL.2020.08.005

Publisher: Elsevier BV

Persistent URL: https://hdl.handle.net/1721.1/132702

Version: Author's final manuscript: final author's manuscript post peer review, without publisher's formatting or copy editing

Published in final edited form as:

Mol Cell. 2020 October 01; 80(1): 29–42.e10. doi:10.1016/j.molcel.2020.08.005.

ppGpp coordinates nucleotide and amino-acid synthesis in *E. coli* during starvation

Boyuan Wang[1], **Robert A. Grant**[1], **Michael T. Laub**[1,2,*]

[1]Department of Biology

[2]Howard Hughes Medical Institute Massachusetts Institute of Technology Cambridge, MA 02139 USA

Summary

(p)ppGpp is a nucleotide messenger universally produced in bacteria following nutrient starvation. In *E. coli*, ppGpp inhibits purine-nucleotide synthesis by targeting several different enzymes, but the physiological significance of their inhibition is unknown. Here, we report the structural basis of inhibition for one target, Gsk, the inosine-guanosine kinase. Gsk creates an unprecedented, allosteric binding pocket for ppGpp by restructuring terminal sequences, which restrains conformational dynamics necessary for catalysis. Guided by this structure, we generated a chromosomal mutation that abolishes Gsk regulation by ppGpp. This mutant strain accumulates abnormally high levels of purine nucleotides following amino-acid starvation, compromising cellular fitness. We demonstrate that this unrestricted increase in purine nucleotides is detrimental because it severely depletes pRpp and essential, pRpp-derived metabolites, including UTP, histidine, and tryptophan. Thus, our results reveal the significance of ppGpp's regulation of purine nucleotide synthesis and a critical mechanism by which *E. coli* coordinates biosynthetic processes during starvation.

Introduction

Guanosine tetraphosphate and pentaphosphate, collectively denoted as (p)ppGpp, is a second messenger that is universally conserved among bacteria (Atkinson et al., 2011). Typically triggered by nutrient starvation, (p)ppGpp synthesis allow bacteria to slow their growth under various adverse conditions (Dalebroux and Swanson, 2012; Potrykus and Cashel, 2008; Potrykus et al., 2011). The ability to both synthesize and degrade (p)ppGpp is critical to the survival of bacteria in a broad range of environmental conditions including, for pathogens, within a host (Dalebroux and Swanson, 2012). High levels of (p)ppGpp promote a so-called persister state, a dormant, non-growing state that renders cells tolerant to antibiotics (Harms et al., 2016). Despite the universality and importance of (p)ppGpp as a growth regulator in bacteria, how it controls cell growth remains incompletely understood.

*corresponding author and Lead Contact: laub@mit.edu.

Author Contributions

B.W. performed all experiments. R.A.G helped with X-ray crystallography for structure determination. B.W. and M.T.L designed experiments, analyzed data, prepared figures, and wrote the manuscript.

Declaration of Interests

The authors declare no competing interests.

(p)ppGpp was first identified and has been best studied following amino-acid starvation in *E. coli*, the so-called stringent response (Cashel and Gallant, 1969). The (p)ppGpp synthase RelA is a ribosome-associated enzyme that can detect uncharged tRNAs in the α-site of the ribosome, as occurs following amino-acid limitation (Haseltine and Block, 1973). In response, RelA uses ATP to pyrophosphorylate GTP, leading to the production of pppGpp, which is typically converted to ppGpp in *E. coli* by the phosphatase GppA (Hara and Sy, 1983). During exponential growth, *E. coli* harbors a baseline, usually low micromolar, level of ppGpp (Wang et al., 2019). Upon acute amino-acid starvation, ppGpp accumulates to millimolar levels within minutes. This ppGpp then reprograms cellular transcription and metabolism by binding to, and modulating the activity of, various target proteins (Hauryliuk et al., 2015; Kanjee et al., 2012). For example, (p)ppGpp directly binds two sites on RNA polymerase (RNAP) in *E. coli* to promote association of the transcription factor DksA and alter promoter specificity, leading to a downregulation of ribosomal RNA transcription while promoting the expression of many biosynthetic genes (Ross et al., 2016; Sanchez-Vazquez et al., 2019).

ppGpp also binds and likely regulates dozens of others proteins (Zhang et al., 2018). We recently used photocrosslinkable variants of ppGpp to systematically identify its binding targets in *E. coli* (Wang et al., 2019). Four of the enzymes identified participate in purine nucleotide synthesis or purine salvage: glutamine amido-phosphoribosyltransferase (PRTase), PurF; hypoxanthine PRTase, Hpt; guanine PRTase, Gpt; and inosine-guanosine kinase, Gsk (Figure 1A, highlighted in red). Together, these enzymes govern all pathways feeding into the synthesis of GTP and almost all pathways leading to the synthesis of ATP (Jensen et al., 2008). (p)ppGpp also downregulates GTP synthesis in *B. subtilis* by directly inhibiting Hpt, Gpt, as well as Gmk, the GMP kinase (Kriel et al., 2012). Collectively, these prior studies indicate that the inhibition of purine nucleotide synthesis is a conserved and likely critical target of (p)ppGpp. However, it remains unclear why bacteria downregulate GTP or ATP synthesis during periods of starvation.

In *B. subtilis*, where (p)ppGpp does not directly regulate RNAP, the downregulation of GTP helps slow the GTP-dependent transcription initiation of ribosomal genes (Krasny and Gourse, 2004), and promote expression of biosynthetic genes via CodY, a transcription factor not found in *E. coli* (Ratnayake-Lecamwasam et al., 2001). Thus, a failure to downregulate GTP in *B. subtilis* could lead to unrestrained ribosomal RNA transcription. However, *E. coli* does not require low GTP to reprogram transcription and it also uses ppGpp to downregulate ATP synthesis, suggesting that the inhibition of purine nucleotide synthesis by (p)ppGpp may have other, likely more conserved, significance.

To better understand the physiological significance of downregulating purine nucleotide synthesis during starvation, we set out to identify and characterize mutations in *E. coli* that selectively ablate ppGpp-dependent regulation of key purine nucleotide synthetic enzymes. To this end, we determined the crystal structure of Gsk in complex with ppGpp, finding that ppGpp binds at an unprecedented, allosteric binding site. Using this structure as a guide, we then constructed an *E. coli* strain encoding a mutant Gsk insensitive to ppGpp and another feedback inhibitor, GDP. When fed Gsk substrates (inosine or guanosine), this strain accumulates abnormally high levels of purine nucleotides, particularly

following the induction of ppGpp during amino-acid starvation. Our metabolomic studies demonstrate that high levels of purine nucleotides, and ADP in particular, strongly represses the synthesis of 5'-phosphoribosyl-1'-diphosphate (pRpp), leading to a shortage of pRpp-derived metabolites including pyrimidine nucleotides, histidine, and tryptophan. We demonstrate that the decrease in these essential metabolites produces significant growth defects, particularly following nutritional downshift. Collectively, our results reveal that the rationale behind ppGpp-dependent inhibition of purine nucleotide synthesis is to permit the synthesis of pRpp and essential, pRpp-derived metabolites.

Results

ppGpp tightly binds to Gsk, inhibits its activity and induces tetramerization

We previously identified Gsk as a putative target of ppGpp using a photo-crosslinkable derivative of ppGpp and mass-spectrometry (Wang et al., 2019). The enzyme Gsk uses ATP to phosphorylate inosine or guanosine into their respective 5'-monophosphate (Figure 1A), with a strong preference for guanosine (K_m = 8 μM) over inosine (K_m = 1.5 mM) (Kawasaki et al., 2000; Mori et al., 1995). GDP, but not GTP or GMP, provides feedback inhibition of Gsk (Kawasaki et al., 2000), and a mutant that escapes feedback inhibition has been isolated but its sequence never reported (Petersen, 1999). Together, these prior findings suggest that GDP and, possibly, the structurally similar molecule ppGpp, bind Gsk at an allosteric site.

To validate Gsk as a ppGpp target, we purified recombinant Gsk and performed isothermal titration calorimetry (ITC). Both GDP and ppGpp bound Gsk at 1:1 stoichiometry (Figure 1B, Table S1). The affinity of Gsk for ppGpp was 100 nM, which is among the tightest affinities known (Steinchen and Bange, 2016) for ppGpp targets and about 20-fold stronger than that for GDP. Using a reaction in which ADP production by Gsk is coupled to NADH consumption by pyruvate kinase (PK) and lactate dehydrogenase (LDH), we found that ppGpp potently inhibited both the inosine- and guanosine-kinase activities of Gsk *in vitro* (Figure S1A). Because GDP is incompatible with the PK-LDH coupling system, we also assayed inosine-kinase activity by coupling formation of inosine 5'-phosphate (IMP) to NADH production using excess IMP dehydrogenase (GuaB) from *E. coli* (Figure 1C), which revealed that ppGpp is a stronger inhibitor than GDP (Figure 1C). Notably, although ppGpp has been reported to inhibit *E. coli* GuaB (Gallant et al., 1971), we did not observe substantial inhibition with ppGpp up to 1 mM (Figure S1B).

In our ITC experiment with Gsk and ppGpp, the heat signal deviates from a single binding-site model at low ppGpp:Gsk ratios suggesting cooperativity between binding sites and/or a change of oligomeric state upon ppGpp binding (Figure 1B). We therefore examined the quaternary structure of Gsk. Using size-exclusion chromatography in tandem with multi-angle light scattering detector (SEC-MALS), we found that Gsk formed dimers in the absence of ppGpp (Mori et al., 1995), but formed tetramers in the presence of 100 μM ppGpp (Figure 1D). This ppGpp-induced tetramerization was nearly complete at Gsk concentrations as low as 2 μM and still significant at 0.5 μM, with the latter being close to the detection limit of our dynamic light-scattering instrument (Figure 1E). GDP also induces Gsk tetramerization, but to a lesser extent than ppGpp, likely due to its weaker affinity (Figure 1E). Collectively, our data show that ppGpp binds, inhibits, and induces the

tetramerization of Gsk, similar to the known feedback inhibitor GDP, except that ppGpp has a higher affinity.

To test whether the inhibition of Gsk by ppGpp was physiologically relevant, we took advantage of the fact that cells expressing a variant of GuaB lacking the so-called CBS domain cannot survive in M9-glucose minimal medium supplemented with inosine (Pimkin et al., 2009a). The growth deficiency of this *guaB*$^{\Delta CBS}$ strain likely results from unregulated Gsk activity in salvaging inosine, leading to a massive accumulation of purine nucleotides (Figure 1F). Consequently, deleting *gsk* can rescue the growth defect of a *guaB*$^{\Delta CBS}$ strain (Pimkin et al., 2009a). Based on our *in vitro* data, we hypothesized that elevated levels of ppGpp should also rescue the defect by inhibiting Gsk (Figure 1F). To test this idea, we transformed the *guaB*$^{\Delta CBS}$ strain with pRelÅ, which expresses a synthetase that produces (p)ppGpp upon addition of IPTG (Schreiber et al., 1991). In M9-glucose, the addition of inosine substantially slowed the growth of cells, as expected (Figure 1G). However, a moderate induction of RelÅ, but not the catalytically inactive RelÅ(D275G), improved the growth rate of *guaB*$^{\Delta CBS}$ cells grown in inosine, with these cells growing at approximately the same rate as cells expressing RelÅ in the absence of inosine (Figure 1G, S1C–E).

To assess whether the growth rescue observed was accompanied by a change in purine nucleotide intermediates, we pulse-treated *guaB*$^{\Delta CBS}$ cells harboring the pRelÅ plasmid with inosine alone or inosine plus IPTG, and then harvested cells for metabolic profiling. In the absence of IPTG, *i.e.* without the production of ppGpp, the addition of inosine led to a significant and sustained accumulation of ATP, GTP, GDP and GMP (Figure 1H–I, S1F–G). Notably, after 10 min of inosine treatment, GDP accumulated up to 0.4 nmol/OD_{600}, or approximately 0.6 mM, 250-fold higher than the K_D value of Gsk-GDP interaction. This level of GDP, however, could not stop further accumulation of purine nucleotides, suggesting that Gsk is somehow stabilized in an active form *in vivo*. In contrast, cells treated with both inosine and IPTG accumulated ppGpp to 0.35 nmol/OD_{600}, about 5,000-fold higher than its K_D value, which effectively suppressed the accumulation of purine nucleotides (Figure 1H–I, S1F–G). We did not detect pppGpp throughout the time course. We conclude that ppGpp functions at physiologically relevant concentrations and is a stronger Gsk inhibitor *in vivo* than GDP.

Gsk restructures both N- and C-termini to bind ppGpp

Gsk is a member of the phosphofructokinase B (PfkB) family, which also contains adenosine kinases (AKs), ribokinases (RKs) and other kinases that phosphorylate a furanose moiety (Park and Gupta, 2008). Gsk homologs comprise a bacteria-specific clade of this family that shares strongest similarity with eukaryotic AKs (Park and Gupta, 2008). Gsk contains all conserved secondary structural elements in AKs, with a few insertions and deletions in loop regions (Figure S2A). This consensus domain, referred to as the AK core hereafter, is flanked by conserved extension sequences on the N- and C-termini. To date, no other PfkB family member has been implicated to interact with ppGpp. Additionally, while RKs and PfkBs are known to form constitutive dimers, AKs normally do not have quaternary structures (Park and Gupta, 2008).

To understand how ppGpp binds and regulates Gsk, we first crystallized Gsk without ppGpp but in the presence of guanosine and ADP, and solved the structure to 1.8Å resolution (PDBID: 6VWO; Table 1). The asymmetric unit contained one Gsk subunits, which was related to its dimeric partner by a two-fold, crystallographic rotational symmetry (Figure 2A). Guanosine and ADP are present at their conserved binding sites near the catalytic center. The dimeric interface locates within the AK core domain and consists of a short α-helix and flanking loops from each subunit (Figure 2A, dashed box). This interface provides intense hydrophobic contact and an octagonal coordination of a K^+ cation (Figure S2B–C). To validate this interface, we disrupted Gsk dimerization by mutating three participating hydrophobic residues into polar ones (I122S/L130K/C131S) (Figure S2D). Using this monomeric Gsk mutant, we confirmed that dimerization is required for Gsk activity, but not ppGpp binding (Figure S2E, Table S1). Notably, the conserved extension sequences on Gsk termini, although present in the protein used for crystallization, were not seen in the ppGpp-free structure due to their conformational flexibility (Figure 2A).

Next, we solved the structure of Gsk bound to ppGpp at 3.4 Å resolution (PDBID: 6VWP; Table 1). The asymmetric unit of this crystal contains four Gsk homodimers (Figure 2B). In agreement with our ITC data, each Gsk subunit bound one ppGpp molecule (Figure 2B–D). ppGpp binding did not induce substantial conformational changes to most of the AK core (residues 33–420), with two exceptions: the ATP-binding loop (residues 344–355, purple in Figure S2F), which adopts a different conformation in the absence of ADP; and a loop (residues 378–385, yellow in Figure S2F), which re-structures to position Lys383 for a critical salt bridge with the 5'-PP_i of ppGpp (Figure 2E, S2G). With these two loops excluded, the Gsk AK core with and without ppGpp aligned closely, with an RMSD = 0.55Å for 368 Ca atoms (Figure S2F).

In contrast to the AK core, ppGpp binding induced dramatic changes in the protein's termini, leading to resolved structure for both extension sequences of Gsk (Figure 2C). Five conserved hydrophobic residues at the extreme N-terminus of Gsk pack against a surface primarily comprised of the last three turns of α-helix-13 of the AK core (Figure 2F). Similarly, the conserved Tyr431-Trp432 dyad clamps the extreme C-terminus to α-helix-14 and the neighboring sequence forms an α-helix (Figure 2F). Both extension sequences contribute important contacts to ppGpp (Figure 2E–F). The side chain of Arg7 and backbone amides of Lys10 provide electrostatic- and hydrogen-bonding to the 5'-β-phosphate of ppGpp. This configuration would occlude the binding of a 5'-triphosphate ligand (Figure S2H) and, in accordance with this idea, pppGpp binds Gsk with a much weaker affinity (Figure S2I and Table S1). The terminal carboxylate (on R434) accepts a hydrogen bond from the Waston-Crick side of the guanine base, providing base specificity (Figure 2E–F). The guanine base is also sandwiched between the side chains of Phe321 and Gln396 via π-stacking, and the N7 atom receives hydrogen bonding from the Ser393 side chain (Figure 2E, S2F). To validate these contacts between ppGpp and Gsk side chains, we used alanine mutagenesis, finding that R7A, F321A, and K383A, S393A and Q396A each rendered Gsk at least 5-fold less sensitive to ppGpp inhibition *in vitro* (Figure 2G). Shortening Gsk by one residue (ΔR434), which withdraws the C-terminal carboxylate away from ppGpp, had a similar effect (Figure 2G).

Gsk also specifically recognizes the distinctive 3'-PP_i group of ppGpp, using side chains of Lys10 and Arg302 (Figure 2D, S2J). Arg302 positions its cationic guanidinium group between the two PPi groups. Although density for the Lys10 side chain was missing beyond Cβ, we infer from its backbone conformation that its side chain should orient towards 3'-PPi for electrostatic interactions. Consistent with this model, Gsk bearing a K10A or R302A mutation had reduced sensitivity to ppGpp, and was no longer more sensitive to ppGpp than GDP (Figure S2K). Importantly, all side chains involved in specific contacts with ppGpp are highly conserved in Gsk orthologs and the C-termini is always two residues away from a Tyr-Trp dyad (Figure S2A), indicating that ppGpp binding is likely a conserved feature of Gsk.

ppGpp inhibits Gsk by blocking conformational dynamics and inducing tetramerization

Given that the conformation of the Gsk AK core is relatively unchanged after ppGpp binding, how does ppGpp binding at an allosteric site inactivate the enzyme? To answer this question, we first considered the conformational dynamics required to complete the catalytic cycle, which has been characterized in detail for *Toxoplasma gondii* AK (Schumacher et al., 2000), a close eukaryotic homolog of Gsk (Figure 3A; see Figure S2A for sequence alignment). This monomeric AK contains two subdomains, and adenosine substrate binds the cleft in between (Figure 3A, left). To release product and bind new substrate, AK must access an open conformation by rotating the large subdomain away from the small one (Figure 3A). In both of our structures, Gsk adopts the guanosine-bound, closed conformation. Despite extensive effort, we could not crystallize Gsk in the absence of a nucleoside substrate. To demonstrate that Gsk exhibits similar conformational dynamics, we introduced a recognition sequence for cleavage by the coagulation factor Xa (FXa), to a region that forms a β-strand in the small subdomain, but should melt into a loop in the open conformation (Figure S3A). As expected, FXa cleaved this engineered Gsk, producing 10- and 38-kDa bands (Figure S3B). Addition of 1 mM guanosine, which should saturate Gsk (Figure S3C), abolished this cleavage (Figure S3B), indicating that releasing ligand from the nucleoside binding site, indeed, drives conformation opening of Gsk. Gsk differs from *T. gondii* AK, however, by dimerizing via an interface that packs against the small subdomain, forming what we will hereafter call the "small and dimerization subdomain (SDD)" (Figure 3B, orange). In our ppGpp-free structure, the large subdomains of Gsk are clearly amenable to rotation away from the SDD and opening of the nucleoside binding cleft (Figure 3B, left). In contrast, ppGpp binding, which structures the N- and C-termini, would effectively block such a rotation (Figure 3B, right) and thereby block Gsk from completing its catalytic cycle.

A prediction from this inhibition model is that ppGpp binding stabilizes the closed, nucleoside-bound conformation of Gsk and *vice versa*. To test this idea, we first examined the affinity of inosine and guanosine to Gsk with or without ppGpp using ITC. Saturating Gsk with ppGpp dramatically enhanced the affinity of both nucleosides (Figure 3C, S3D, Table S1). Using the low-affinity inosine as substrate, we then examined the competitiveness of ppGpp inhibition. Strikingly, high concentrations of inosine enhanced the potency of ppGpp (Figure 3D). Lineweaver-Burk plotting indicated that ppGpp is a counter-competitive, or cooperative, inhibitor with respect to inosine (Figure S3E). With ppGpp above 100μM, Gsk activity increased with lower inosine—a behavior not conforming

to Michaelis-Menten kinetics. In agreement with this cooperativity between ppGpp and nucleoside binding, pre-saturating Gsk with guanosine also enhanced the affinity of GDP or ppGpp (Figure S3F, Table S1). The binding heat of ppGpp was 10.8 kcal/mol more favorable when Gsk was bound to guanosine, which was reasonably close to the 8.7 kcal/mol gain for guanosine binding when Gsk is bound to ppGpp (Figure S3D, S3F, Table S1). Similar cooperativity was not observed with respect to the other Gsk substrate, ATP. Instead, ppGpp acts as a mixed-type inhibitor, and is more potent with lower concentration of ATP (Figure 3E, S3G).

In addition to structuring the N- and C-termini, ppGpp restrains conformational dynamics of Gsk also by inducing tetramerization. In the Gsk-ppGpp co-crystal, four homodimers form a ring-shaped octamer in the asymmetric unit (Figure S3H). Given that Gsk-ppGpp is tetrameric in solution (Figure 1D–E), we propose that the octamerization is an artifact due to the extreme protein concentrations used for crystallization. In accord with this notion, of four interfaces between dimers within the crystallographic octamer, three are roughly equivalent, and each buries a larger surface area than the fourth (1380 vs 660 $Å^2$, Figure S3I). This more extensive interface is likely responsible for ppGpp-induced tetramerization (Figure 3F). Leu308 and Glu315 of one subunit form three hydrogen bonds to Lys10 and His11 from the opposite subunit, which are positioned by direct contact with ppGpp (Figure 3G, S2A). Each tetramer is supported by two copies of these interactions related by a two-fold axis of symmetry (Figure 3F). To validate the role of these contacts in tetramer formation, we mutated Leu308 to serine, which should destabilize the conformation of the proximal His11 and Glu315 side chains. As expected, this mutation abrogated tetramerization (Figure 3H) without affecting affinity to ppGpp (compare Figure S3J to 1B, Table S1).

Tetramerization, which involves the large subdomain of each Gsk monomer, should further rigidify the closed conformation of Gsk (Figure 3F, I). We therefore expected that ppGpp-bound Gsk would be less active as a tetramer than as a dimer. DLS data suggest that Gsk-ppGpp is ~67% tetrameric at 500 nM monomeric concentration (Figure 1E, Methods). Thus, 50 nM Gsk-ppGpp should be ~70% dimeric. At this concentration, WT and the L308S mutant had similar responses to ppGpp inhibition (Figure 3J). Increasing protein concentration from 50 nM to 6 μM should significantly increase the fraction of tetramers in the population of WT, but not the L308S mutant, Gsk-ppGpp complex (Figure 3K). We therefore measured guanosine-kinase activity at a series of Gsk concentrations in the presence of saturating levels of ppGpp and guanosine (1 mM each, Figure 3K). As predicted, the specific activity of WT Gsk decreased with higher enzyme concentration, indicating that the Gsk-ppGpp tetramers are less active than dimers. In contrast, the specific activity of the dimer-only Gsk(L308S) stayed relatively constant within this concentration range. Taken all together, we conclude that ppGpp inhibits Gsk by preventing the opening of the nucleoside-binding cleft through two layers of steric hinderance: (i) the induced structuring of terminal extension sequences and (ii) tetramerization (Figure 3I).

Feedback inhibition of Gsk maintains a balance between purine and pyrimidine synthesis

Our structural studies produced several Gsk mutants insensitive to ppGpp inhibition, including Gsk(K383A), which is completely insensitive to ppGpp and GDP (Figure 2F, S4A). To test the physiological significance of Gsk regulation by ppGpp and GDP, we introduced the K383A mutation into the chromosomal *gsk* locus in *E. coli*. As expected, *gsk*(K383A) had no obvious, deleterious phenotype in the growth medium M9-glucose containing casamino acids (M9GC) (Figure 4A–B). However, adding inosine or guanosine to the medium led to moderate or severe growth defects, respectively (Figure 4A–B), though no change in viability (Figure S4B). These results support the notion that an inability to regulate the activity of Gsk disrupts purine homeostasis and, consequently, growth.

To better understand the molecular basis for the defects observed in the Gsk(K383A) mutant, we plated *gsk*(K383A) cells on M9GC containing guanosine and selected the spontaneous suppressors that arose (Figure S4C). We sequenced the genomes of 11 suppressors (Table S2). Two suppressors mapped to *gsk*, leading to reduced activity and poor folding of Gsk, respectively (Figure S4D–E). Intriguingly, 8 of 11 sequenced suppressors had single-nucleotide mutations in the attenuator element upstream of the *pyrE* gene encoding orotate PRTase, a pRpp-utilizing enzyme involved in the *de novo* synthesis of UTP (Figure 4C–D, Table S2) (Bonekamp et al., 1984; Jensen et al., 2008). All of these mutations in the *pyrE* attenuator are predicted to destabilize the stem-loop and thereby enhance the expression of *pyrE* (Figure 4C). Four of the suppressors with *pyrE* mutations had no other chromosomal mutations, and we selected one of them for further study and comparison to the parental, *gsk*(K383A) strain (Entry 5, Table S2). We first confirmed, using qRT-PCR, that *pyrE* levels were, in fact, elevated in the *pyrE* suppressor strain (Figure 4E).Additionally, we used in-lysate biochemical assays to show that PyrE activity was elevated in the suppressor strain relative to the wild-type and parental *gsk*(K383A) strains (Figure 4F) (Jensen, 1979; Schwartz and Neuhard, 1975). We therefore named the suppressive genotype "*pyrE++*".

These data indicated that PyrE activity becomes limiting in the *gsk*(K383A) strain when guanosine or inosine was added to the growth medium. Consistent with this conclusion, we found, using metabolomics, that two pyrimidine precursors, orotate and carbamoyl aspartate, accumulated in the *gsk*(K383A) mutant, whereas the PyrE product OMP, as well as UTP levels, dramatically decreased following addition of purine nucleosides to the medium, particularly guanosine (Figure 4G–H). This depletion of UTP was accompanied by sharp decreases in UDP-GlcNAc and UDP-hexose, which are required for cell-wall and cell-envelope synthesis, respectively (Figure S4F). In contrast to the *gsk*(K383A) strain, the suppressor strain no longer accumulated pyrimidine precursors and had restored the levels of OMP and UTP, as well as UDP-GlcNAc and UDP hexose, even when guanosine or inosine was added to the growth medium (Figure 4G–H, S4F). These results indicate that *pyrE*++ suppresses the growth defect of the *gsk*(K383A) mutant by expanding UTP synthesis capacity.

Following treatment of the *gsk*(K383A) strain with guanosine or inosine, our metabolomics data also revealed an accumulation of ADP, ATP, and GTP concomitant with the decrease of UTP (Figure 4H). High levels of ADP have been suggested to antagonize UTP production

by inhibiting PrsA, the enzyme that synthesizes pRpp, a precursor of UTP (Figure 4D, G) (Hove-Jensen et al., 1986; Petersen, 1999; Pimkin et al., 2009b). In agreement with this idea, we observed a strong decrease in pRpp, a substrate for PyrE, in *gsk*(K383A) cells treated with guanosine or inosine (Figure 4G). Thus, our results suggest that the unregulated activity of Gsk harboring the K383A substitution leads to increased levels of purine nucleotides, including ADP, which inhibits the synthesis of pRpp, limiting the activity of PyrE and the synthesis of UTP. To test this model, we asked whether adding uridine to the medium, which allows UTP synthesis independent of pRpp (Figure 4D) would rescue the slow growth of *gsk*(K383A) cells in the presence of guanosine. Indeed, we found that adding uridine and guanosine simultaneously to the *gsk*(K383A) strain enabled robust growth (Figure 4I). Taken together, our results demonstrate that feedback inhibition of Gsk is required to maintain a balance of purine and pyrimidine nucleotide synthesis. It is, however, difficult to say whether the phenotypes of the *gsk*(K383A) strain arise from an inability of GDP or ppGpp to regulate Gsk. In the growth conditions tested thus far, GDP levels are higher (Figure S4G), but ppGpp is a more potent inhibitor and basal levels of ppGpp (~10 μM) may be high enough for it to control Gsk (Figure 1C).

Unrestricted Gsk activity during the stringent response represses the synthesis of pRpp-dependent amino acids

To better dissect the significance of ppGpp-dependent inhibition of purine nucleotide synthesis via Gsk, we compared the behavior of *gsk*(K383A) and wild-type cells following a downshift from amino acid (AA)-replete to AA-free media, which induces the stringent response and high levels of ppGpp (Figure 5A). For these experiments, we added inosine to drive flux through Gsk(K383A) as well as uridine to prevent the UTP limitation described above. The *gsk*(K383A) and wild-type strains grew at indistinguishable rates in both AA-replete and AA-free media (Figure S5A). However, the *gsk*(K383A) strain recovered much more slowly after undergoing AA downshift (Figure 5B), presumably as a consequence of unrestricted Gsk activity following ppGpp induction. In agreement with this idea, we observed a significant accumulation of ATP and GTP levels in *gsk*(K383A) cells within ~30–60 minutes after the downshift (Figure 5C, S5B). ADP levels increased concomitantly with ATP, leading to a substantial depletion of pRpp in *gsk*(K383A) cells relative to wild-type cells (Figure 5D, S5B), consistent with ADP-mediated downregulation of the pRpp synthase, PrsA. UTP levels were unaffected as its synthesis from exogenous uridine no longer requires pRpp (Figure 5C, 4D).

Although ppGpp is synthesized from ATP and GTP, higher levels of these substrates in *gsk*(K383A) did not lead to increased ppGpp accumulation post-downshift (Figure 5C). However, ppGpp levels persisted for longer in the *gsk*(K383A) mutant compared to the wild type (Figure 5C). Based on this observation, we suspected that the mutant strain may have trouble synthesizing one or more amino acids and therefore continued to produce ppGpp. In light of this idea, we surveyed our metabolomics data for signals of all 19 detectable AAs (except cysteine) as a function of time post-downshift (Figure 5E and S5C). Remarkably, the levels of histidine and tryptophan, which both require pRpp for their biosynthesis (Hove-Jensen et al., 2017), were lower in *gsk*(K383A) cells throughout the time course and, more importantly, remained lower at 210-min post-downshift (Figure 5E), when *gsk*(K383A) cells

first showed higher ppGpp and a growth deficiency relative to wild-type cells (Figure 5B–C).

Strikingly, we found that adding just these two AAs - histidine and tryptophan - to the destination medium (otherwise AA-free), allowed *gsk*(K383A) cells to achieve the same growth rate as wild-type cells recovering from the downshift (Figure 5F–G), with the mutant cells no longer maintaining high levels of (p)ppGpp after significant re-growth is achieved (Figure 5H, see Methods for details). Importantly, the mutant cells still accumulate higher levels of purine nucleotides (Figure S5D), particularly ADP (Figure 5I, S5B), in the first two hours after AA downshift indicating that the excess purine nucleotide levels *per se* do not result in a growth phenotype of *gsk(K383A)* cells following AA downshift. Two other AA combinations, one containing phenylalanine and tyrosine and the other containing isoleucine, leucine and valine (none of which require pRpp for synthesis) did not enable *gsk*(K383A) cells to recover as fast as wild-type cells after AA-downshift (Figure 5F–H). Collectively, our results reveal a key rationale behind the inhibition of purine nucleotide synthesis by ppGpp during the stringent response: cells must minimize the accumulation of purine nucleotides, in particular ADP, to maintain the synthesis of pRpp and critical pRpp-derived metabolites such as histidine and tryptophan (Figure 6).

Discussion

The rationale behind inhibiting purine-nucleotide synthesis during the stringent response

(p)ppGpp has been known to target purine nucleotide synthesis for decades, but the significance of this regulation during the stringent response has remained unclear. Early work in *E. coli* demonstrated that the purine salvage enzymes Gpt and Hpt are inhibited by (p)ppGpp *in vitro* (Hochstadt-Ozer and Cashel, 1972), and our recent efforts to systematically identify (p)ppGpp targets in cell lysates confirmed Gpt and Hpt as targets while identifying PurF and Gsk as putative new targets (Figure S6A) (Hochstadt-Ozer and Cashel, 1972; Wang et al., 2019). pppGpp also activates the nucleosidase PpnN to cleave purine nucleoside monophosphates (Figure S6A) (Zhang et al., 2019). Thus, *E. coli* has evolved to ensure that purine nucleotide levels are tightly regulated during the stringent response, but the rationale underlying this regulation has remained elusive.

Here, we demonstrated that the downregulation of purine nucleotide synthesis is critical for cells to conserve pRpp, a common precursor required for the synthesis of purine and pyrimidine nucleotides, the amino acids histidine and tryptophan, as well as NAD, which could be produced from tryptophan (Hove-Jensen et al., 2017). ADP is the only known inhibitor of PrsA, the pRpp synthetase in *E. coli* (Hove-Jensen et al., 2017; Hove-Jensen et al., 1986). When we subjected our mutant strain expressing *gsk*(K383A), which is blind to ppGpp, to a nutrient downshift, cells accumulated more purine nucleotides, including ADP, leading to a sustained decrease in pRpp, histidine, and tryptophan. The decrease in these amino acids led to a much slower growth recovery compared to wild-type cells. Strikingly, this growth defect was completely rescued by adding histidine and tryptophan to the destination medium (Figure 5F). Thus, our findings indicate that ppGpp acts to restrict the accumulation of purine nucleotides, specifically ADP, to prevent the inhibition of PrsA and to maintain sufficient pRpp for the synthesis of other, essential metabolites. This

restriction of purine nucleotide synthesis results from the multiplicity of ppGpp targets, with an inhibition of Gsk being particularly important in the presence of inosine or guanosine (Figure 1A, 6, S6A).

The downregulation of purine nucleotide synthesis is likely particularly critical during the stringent response because (p)ppGpp also inhibits bulk RNA synthesis (Potrykus and Cashel, 2008), the main cellular activity that consumes purine nucleotides. Purine nucleotides are thus prone to accumulation, unless synthesis is also inhibited. We propose that this demand for a safeguard mechanism drove the evolution of strong inhibitory interactions between (p)ppGpp and the enzymes PurF, Gpt, Hpt, and Gsk in *E. coli* (Figure S6A). Taken all together, our results provide a clear metabolic rationale behind the ppGpp-dependent inhibition of purine nucleotide synthesis, while also underscoring the central metabolic role of pRpp, particularly during times of starvation.

The targeting of purine nucleotide synthesis by (p)ppGpp is conserved, although the enzymes targeted seems to vary (Figure S6A) (Liu et al., 2015). While Gpt and Hpt are direct targets in both *E. coli* and *B. subtilis* (Anderson et al., 2019; Hochstadt-Ozer and Cashel, 1972), PurF is not (Figure S6B), and a Gsk ortholog is not found in *B. subtilis*. Instead, *B. subtilis* uses (p)ppGpp to directly inhibit Gmk to block GTP synthesis (Kriel et al., 2012). For *B. subtilis* and possibly other Gram-positive species, the inhibition of guanine salvage enzymes is essential even in the absence of starvation, i.e., by a baseline level of (p)ppGpp, and helps to prevent a phenomenon called ‘death by GTP’ (Kriel et al., 2012). However, why excess GTP is detrimental in *B. subtilis* is not known. Our results indicated that high GTP levels *per se* were not lethal to *E. coli*: excess guanosine salvage by Gsk(K383A) inhibited cell growth, but did not lead to a detectable loss of viability (Figure S4B). Moreover, the growth defect of the *gsk(K383A)* mutant following nutrient downshift was completely suppressed by adding uridine, histidine, and tryptophan to the medium even though purine nucleotide levels remained high. Despite different levels of tolerance to excess purine nucleotide levels, it is clear that downregulating purine nucleotide synthesis and salvage is a key facet of the stringent response in both *E. coli* and *B. subtilis*, and likely most bacteria.

Several other steps of purine metabolism have been previously implicated in regulation by (p)ppGpp. For instance, earlier studies claimed that adenylosuccinate synthase, PurA, and IMP dehydrogenase, GuaB, are direct targets of ppGpp in *E. coli*. PurA and GuaB control the first step of ATP and GTP synthesis from IMP, respectively (Figure S6A) (Gallant et al., 1971). We could not reproduce the inhibition of GuaB by ppGpp *in vitro* (Figure S1B), but we did confirm that ppGpp can inhibit PurA, though only as a weak (K_D = 61 μM by ITC) competitor with respect to GTP (Figure S6C–D). More importantly, the *gsk*(K383A) strain, despite harboring wild-type PurA and GuaB, effectively accumulated both ATP and GTP following nutrient downshift (Figure 5C). Together, these results indicate that PurA and GuaB are not critical *in vivo* targets of ppGpp, or at least are secondary to Gsk.

Structural basis of ppGpp-dependent regulation

Our studies of Gsk have also now revealed a new mode of binding and inhibition by (p)ppGpp. We found that the N- and C-terminal sequences of Gsk were disordered in the

absence of ppGpp, but were structurally resolved in the presence of ppGpp (Figure 2). Both termini pack against the AK core of the protein and make crucial contacts with ppGpp. In particular, N-terminus and the core domain use several positively charged residues to electrostaticically accommodate the 5'-diphosphate on ppGpp. The C-terminal carboxylate provides base discrimination through two hydrogen bonds with the Watson-Crick side of guanine. The binding of ppGpp to Gsk also induced tetramerization. ppGpp binding inhibits Gsk by ~60 fold (Figure 3J), with tetramerization further inhibiting it ~5 fold (Figure 3K). The key residues involved in ppGpp binding and tetramerization are both highly conserved (Figure S2A), suggesting that both layers of regulation are important.

In general, there appears to be a great diversity of ways in which ppGpp can bind target proteins (Steinchen and Bange, 2016). For certain GTPases and PRTases, (p)ppGpp simply occupy conserved binding site for GTP or pRpp as a structural mimicry (Anderson et al., 2020; Anderson et al., 2019; Buglino et al., 2002; Fan et al., 2015; Pausch et al., 2018). But for those enzymes that it regulates allosterically, no common mechanism or structural motif has emerged yet, beyond the expected involvement of positively charged residues that coordinate the multiple phosphates of ppGpp. Thus, efforts to predict allosteric ppGpp binding sites may not be feasible. Conversely, however, the diversity of binding sites may reflect the relative ease with which ppGpp binding and regulation can arise during evolution, which may help explain why ppGpp targets different proteins in different organisms.

Coordinating different metabolic pathways during nutrient starvation

The stringent response orchestrated by ppGpp is critical to the survival of most bacteria on the planet, and is often required for full virulence of pathogens inside their hosts given its central role in controlling growth rate. The tuning of growth rate by ppGpp requires that it coordinately regulate nearly all cellular biosynthetic processes, not just RNAP and transcription. Indeed, recent studies have revealed many different proteins involved in many different metabolic pathways and cellular processes that are likely directly targeted by ppGpp. Our work has validated purine nucleotide biosynthesis as a major target of ppGpp and revealed the underlying rationale. It is not the suppression of ATP and GTP *per se* that appears important, but rather that ADP levels must be restrained to permit PrsA-dependent synthesis of pRpp, which feeds the synthesis of essential metabolites, including pyrimidines, histidine, tryptophan, and NAD. Thus, our work indicates that ppGpp does not just downregulate individual pathways, but it orchestrates a true reprogramming of metabolism to promote survival. Such sophisticated coordination of metabolism is likely critical throughout the bacterial kingdom, with additional layers and mechanisms of regulation remaining to be discovered.

STAR Methods

RESOURCE AVAILABILITY

Lead Contact—Questions about or requests for methods, strains, and resources generated in this study can be directed to the Lead Contact, Michael T. Laub (laub@mit.edu).

Materials Availability

Plasmids and strains generated in this study are available upon request to the Lead Contact.

Data and Code Availability

Crystal structures of Gsk in complex with guanosine and ADP and in complex with guanosine and ppGpp are available at RCSB Protein Data Bank, accession codes 6VWO and 6VWP, respectively. The LC-MS data for metabolite profiling are available from the Lead Contact upon request.

EXPERIMENTAL MODEL AND SUBJECT DETAILS

Escherichia coli was grown in LB (10 g/L NaCl, 10 g/L tryptone, 5 g/L yeast extract) or M9-based defined media. All solid media contained 1.2% agar. M9 base medium (14 g/L Na_2HPO_4-$7H_2O$, 3 g/L KH_2PO_4, 0.5 g/L NaCl, 1 g/L NH_4Cl, 1 mM $MgSO_4$, 30 μM $CaCl_2$, 25 μM $Fe(SO_4)$-EDTA chelate, was made into defined media by supplementing nutrients as follows, unless noted otherwise: glucose: 0.4% (w/v); casamino acids: 0.2% (w/v); inosine: 5 mM in liquid, 2 mM in agar; guanosine (as sodium salt): 2 mM; uridine: 2 mM; individual amino acids: 0.01% (w/v). Agar plates were incubated at 37 °C unless noted otherwise. Large cultures (> 10 mL) were grown in Erlenmeyer flasks at 37 °C and 200 rpm on an orbital shaker, and OD_{600} measurements were taken using a 1-cm plastic cuvette. If necessary, the culture was diluted to OD_{600} < 0.4 and the dilution was factored in. For high-throughput growth curve recording, cultures were grown in 96-well plates (100 μL wells, Figure 1G, and S1D–E) or 24-well plates (1 mL, Figure 4B, 4I, S5A) at 37 °C and 307 rpm in a Synergy H1 plate reader (BioTek).

METHOD DETAILS

Plasmid Construction

All primers and plasmids used are listed in Table S3 and Table S4, respectively.

Sub-cloning: We used Gibson-assembly (Gibson et al., 2009) to ligate vector and insert DNA each of which were PCR-amplified using primers containing appropriate overhangs to ensure ligation specificity. All PCR reactions were performed using the Phusion→ High-Fidelity DNA Polymerase (NEB) kit following the instructions enclosed. PCR products were purified with agarose gel-electrophoresis followed by gel extraction prior to ligation. Circular plasmids were extracted from positive transformants and the presence of correct insert confirmed through Sanger sequencing.

The *E. coli gsk* open reading frame (ORF) (G24–1 in Tables S3–S5) was sub-cloned into pET28b between NdeI and XhoI restriction sites, or into pET Sumo vector (Invitrogen) immediately downstream to the 5'-end of the His_6-Sumo ORF. The *E. coli purA* ORF (G27–1 in Tables S3–S5) was sub-cloned into pET28b vector between NcoI and XhoI restriction sites. The *E. coli guaB* ORF (G30–1 in Tables S3–S5) was sub-cloned into pET Sumo vector immediately downstream to the 5'-end of the His_6-Sumo ORF. Coding sequence of the mature form of *B. subtilis* PurF (residues 12–476 of the entire ORF, added initiating ATG,

G24–2 in Tables S3–S5) was sub-cloned into the backbone of pRelÅ (Table S4) (Wang et al., 2019) between the EcoRI and HindIII site and the first codon of the Cfa-intein ORF.

Site-directed mutagenesis: To introduce point mutations, the template plasmid was PCR-amplified using primer pairs bearing the desired mutation (Table S3) and each PCR reaction was treated with DpnI prior to transformation into *E. coli* DH5a. Mutant plasmids were extracted from transformants selected on LB plates containing carbenicillin. Deletion of the C-terminal Arg434 from the gsk ORF was achieved by sub-cloning. Note that expression plasmids for Gsk suppressor mutants (L105F/K383A and D279V/K383A) were generated by sub-cloning from suppressor strains.

Strain Construction

All strains created are listed in Table S5.

Construction of gsk(WT), ML3271 and gsk(K383A), ML3272: A DNA segment spanning *gsk*(370–434), the T7 terminator and the Kan^R cassette was amplified with primers "G24–1 A370 FP" and "K383:kanR RP" (Table S3) from the Gsk(K383A) expression vector constructed in pET28b. This amplicon was purified with agarose gel-electrophoresis followed by gel extraction, and electroporated into MG1655 (ML006) harboring pKD46 (Datsenko and Wanner, 2000). Note that recipient cells had to be grown in M9-casamino acids containing 1 mM arabinose before being made electrocompetent. Recombinants were selected on M9-glucose-casamino acids (M9GC) agar containing 10 μg/mL kanamycin and incubated at 37 °C to drive the loss of pKD46 and then re-streaked on M9GC agar containing 25 μg/mL kanamycin. Sanger sequencing of *gsk* loci amplified from 12 recombinants detected 6 loci with the K383A mutation and 6 without. One clone of each genotype was grown in M9GC for whole-genome sequencing, which revealed no additional changes elsewhere in the chromosome.

Construction of $guaB^{\Delta CBS}$: The $guaB^{\Delta CBS}$ strain (ML2910), was constructed in an MG1655 (ML006) background through Lambda recombineering following literature-described procedures (Pimkin and Markham, 2008). Briefly, ML006 harboring pKD46 and expressing the Lambda recombinase was electroporated with a kanamycin resistance-cassette (kan^R) fragment amplified from pKD4 with primers "GuaB dCBS FPL" and "GuaB dCBS RPL". Recombinants were selected on LB plates containing 10 μg/mL kanamycin and incubated at 37 °C to drive the loss of pKD46. Then, a recombinant clone was transformed with pCP20 to flip out the kan^R cassette (Cherepanov and Wackernagel, 1995). Transformants were selected on LB plates containing carbenicillin at 30 °C and re-streaked on M9GC plates for growth at 42 °C to confirm purine autotrophy and drive the loss of pCP20. Deletion of the CBS domain from the *guaB* open-reading frame (ORF) was confirmed by Sanger sequencing.

Recombinant proteins

Protein expression: with the exception of *B. subtilis* PurF, all recombinant proteins were expressed in *E. coli* BL21(DE3) harboring the corresponding expression plasmid. Expression strains were grown in LB containing the appropriate antibiotics at 37 °C to

OD_{600} = 0.6. The culture was then cooled to 18 °C and induced by the addition of 200 μM IPTG. Cells were harvested 16 to 24 hours post-induction. *B. subtilis* PurF was expressed as described by Makaroff et al. (Chen et al., 1997). G23–2pTac plasmid was transformed into the *purF:kan*^{R} strain from the KEIO collection (Baba et al., 2006). The transformant was cultured at 37 °C in M9G minimal medium supplemented with 0.2% casamino acids and 100 μg/mL carbenicillin and induced by the addition of 200 μM IPTG at OD_{600} = 0.002. Cells were harvested after shaking at 37 °C for another 20 hours.

Purification of His-tagged proteins: His-tagged proteins were purified following the standard protocol described below. The cell pellet from 50 mL of expression culture was resuspended in 5 mL lysis buffer containing 50 mM Tris-HCl pH = 8.0, 150 mM KCl, 1 mM TCEP, 20 μg/mL lysozyme, 10 units Benzonase (MilliporeSigma) and 1 mM PMSF. Cells were disrupted through sonication and the lysate was cleared at 12,000 *g* for 1 hour. Cleared lysate was applied to 1 mL Ni-NTA resin equilibrated with the lysis buffer, and allowed to flow through by gravity. The Ni-NTA resin was washed with 5x column volumes of wash buffer 1 (50 mM Tris-HCl pH 8.0, 500 mM KCl, 10 mM imidazole and 1 mM TCEP) and 10x column volumes of wash buffer 2 (50 mM Tris-HCl pH 8.0, 150 mM KCl, 25 mM imidazole 1 mM TCEP). Bound protein was eluted with 3X column volumes of elution buffer (50 mM Tris-HCl pH 8.0, 150 mM KCl, 300 mM imidazole and 1 mM TCEP.

Removal of affinity tags: All proteins in this study were removed from affinity tags prior to usage for crystallography and biochemical/biophysical experiments. To remove the N-terminal His_6 tag of recombinant proteins expressed from the pET28b vector, thrombin (Sigma) was reconstituted in 20 mM Tris-HCl pH 8.0, 150 mM NaCl and 20% (v/v) glycerol at 100 U/mL. Eluates off the Ni-NTA column were dialyzed against 20 mM Tris-HCl pH 8.0 and 150 mM KCl, and then treated with thrombin (10 U per μmol cleavage sites) at RT overnight. Upon confirming completion of cleavage using SDS-PAGE, the protein was concentrated, treated with 10 mM TCEP, and refined over a Superdex-200 increase (10/300) column. To remove the N-terminal His_6-Sumo tag, proteins off the Ni-NTA column were exchanged into 20 mM Tris-HCl pH 8.0, 150 mM KCl and 1 mM TCEP. The tagged protein was then treated with Sumo protease (10 μg per μmol cleavage sites) at RT for 2 hrs. The cleavage mixture was subjected to a reverse Ni-NTA process to clean up residual uncleaved protein. Flow-through containing cleaved protein was then concentrated and refined over a Superdex-200 increase (10/300) column (for Gsk) or Superose-6 increase (10/300) column (for GuaB). To remove the C-terminal Cfa-His_6 fused to *E. coli* PurF, Ni-NTA eluate was exchanged into 20 mM HEPES-Na pH 7.0, 150 mM NaCl, and 1 mM TCEP, and treated with 100 mM sodium 2-mercaptoethanesulfonate (MESNa), 100 mM L-cysteine and 20 mM TECP at pH 7.0 and RT overnight. Note that this treatment substituted a Cys residue for the Cfa-His_6 tag (Wang et al., 2015). The cleavage mixture was then extensively dialyzed against the intein-cleavage buffer and then subject to a reverse Ni-NTA process. Flow-through containing cleaved protein was then concentrated and refined over a Superdex-200 increase (10/300) column.

Purification of PurA and B. subtilis PurF: Both proteins were expressed in its exact sequence without affinity tag, and were purified following similar strategies, as exemplified

by *E. coli* PurA as follows. Cell pellet from 1 L expression culture (wet weight ~ 10 grams) was resuspended in 40 mL lysis buffer containing 50 mM Tris-HCl pH 8.0, 50 mM NaCl, 10 mM $MgCl_2$, 5 mM DTT, 20 μg/mL lysozyme and 1 mM PMSF. Cells were disrupted through sonication and the lysate was cleared at 15,000 *g* for 10 min. The supernatant was then treated with 75 mg protamine sulfate and cleared again at 30,000 *g* for 1 hour. Supernatant was applied to a DEAE sepharose column (16/150, ~30 mL bed volume) equilibrated with buffer A (50 mM Tris-HCl pH 8.0, 10 mM $MgCl_2$ and 5 mM DTT). Bound protein was fractionated using a linear gradient of NaCl. PurA was precipitated from combined peak fractions at 0 °C by increasing $(NH_4)_2SO_4$ from 55% to 65% saturation. This PurA pellet was re-dissolved and refined over a Superdex-200 increase (10/300) column.

Procedures for the purification of *B. subtilis* PurF proteins were otherwise identical with the following modifications. Firstly, buffer A in the DEAE-Sepharose chromatography step contained 50 mM Tris-HCl pH 8.0, 10 mM MgCl2, 0.1 mM EDTA, 1 mM AMP-Na and 5 mM DTT, which was also used as lysis buffer with supplementation of 1 mM PMSF (Chen et al., 1997). Pure protein was precipitated by increasing $(NH_4)_2SO_4$ saturation from 30% to 40%.

Size-exclusion chromatography (SEC): SEC of all recombinant proteins was run in buffers containing 20 mM HEPES-Na pH 7.0, 150 mM NaCl (for PurF and PurA) or KCl (for GuaB and Gsk), and 1 mM TCEP. Up to 10 mg protein was injected in 1 mL and peak fractions were combined.

X-ray crystallography

Note that all Gsk protein used for crystallization has a 3-residue, Gly-Ser-His scar sequence on the N-terminus as a result of thrombin cleavage to release the His tag.

Gsk-guanosine-ADP complex: Gsk protein was concentrated to ~1 mM stock, then diluted to 550 μM by mixing with appropriate amount of HBKT buffer, $MgCl_2$ (1M stock in water, 10 mM final concentration), ppGpp (100 mM stock in water, 5 mM final concentration), ADP (100 mM stock, 5 mM final concentration) and guanosine-KOH (1:1, 100 mM stock in water, 5 mM final concentration), in this order. Crystals were grown by hanging drop vapor diffusion with 2 μL protein containing ligand mixed with 2 μL of well solution (0.1 M Tris-HCl pH 8.9, 15% PEG4000 and 0.2M $CaCl_2$) at 18 °C. ppGpp immediately precipitated out with Ca^{2+}. After 10 days crystals were looped out, dipped in well solution containing 25% PEG4000 and 12% glycerol, and frozen in liquid nitrogen.

Diffraction images were indexed, integrated and scaled using HKL2000 (Otwinowski and Minor, 1997). Phaser (McCoy et al., 2007) was used to solve the structure by molecular replacement. A 2.35Å data set collected on a Rigaku Micromax-007HF rotating anode with Varimax-HF mirrors and a Saturn 944 CCD detector was used for initial phasing and refinement. The search model for molecular replacement was an ensemble of models derived from the A chains of PDB entries 5KB5, 2A9Y, 3UBO, 2I6A, 2NWH, 4K8P, 3UQ6 and 3EWN. These entries were identified by the Dali server (Holm and Laakso, 2016) as having structural homology to 5KB5, which exhibits a weak sequence homology to the AK domain of Gsk (33–420). The different components of the ensemble were aligned to the 5KB5

chain in COOT (Emsley et al., 2010) using the secondary structure alignment tool. This alignment identified a structurally conserved core in all the models. Regions outside this conserved core were removed and the trimmed models were realigned to 5KB5 to produce the components of the ensemble that was used as a search model input to Phaser. The Phaser solution was built out using Phenix.autobuild (Adams et al., 2010) and refined in Phenix to $R_{work/free}$ of 0.21/0.26 using the rotating anode data. Final refinement was against a 1.78 Å data set collected on the Pilatus6MF detector at APS/NE-CAT beamline 24-ID-C. COOT was used to adjust the model between each cycle of refinement. The N-terminal 30 amino acids and the C-terminal 23 amino acids of the sequence were not ordered in the crystal and are not present in the final model.

Gsk-guanosine-ppGpp complex: Gsk protein was diluted to 550 μM by mixing with appropriate amount of HBKT buffer, $MgCl_2$ (1M stock in water, 10 mM final concentration), ppGpp (100 mM stock in water, 5 mM final concentration) and guanosine-KOH (1:1, 100mM stock in water, 5 mM final concentration), in this order. Crystals were grown by hanging drop vapor diffusion with 2 μL protein containing ligand mixed with 2 μL of well solution (0.2 M Na-acetate pH 4.8 and 3.1M sodium formate) at 18 °C. After 180 days crystals were looped out and frozen in liquid nitrogen without any cryo-protection. Diffraction data extending to 3.4 Å were collected on the Eiger 16M detector at the APS/NE-CAT 24-ID-E beamline. The structure was solved with Phaser searching for eight copies of a single chain from the partially refined model of the ppGpp-free Gsk. The N and C termini of the protein and the bound ppGpp were built into the resulting map using COOT. The structure was refined with Phenix.

Surface area buried between neighboring Gsk homodimer in the ppGpp-bound crystal was calculated using ‘Protein interfaces, surfaces and assemblies’ service (PISA) (Krissinel and Henrick, 2007) at - http://www.ebi.ac.uk/pdbe/prot_int/pistart.html.

Isothermal Titration Calorimetry (ITC)

All ITC experiments were performed in a VP-ITC (Malvern) instrument thermo-equilibrated at 25 °C with pure water in the reference cell. All Gsk proteins used here were purified as His_6-Sumo fusions followed by traceless release of the Sumo tag. All ligands and proteins are in the same buffer containing 20 mM HEPES 7.4, 150 mM KCl, 1mM TCEP. Additives was present in both buffers at free concentrations indicated in Table S1. For all titrations using 100 μM ligand and 10 μM protein, or 1 mM ligand and 100 μM protein, the ligand was injected at 10 μL/injection for altogether 27 injections. For the titration of 200 μM PurA using 2 mM ppGpp or 100 μM Gsk using 2 mM inosine, the ligand was injected at 5 μL/injection for 55 injections. Blank titrations were performed with protein-free buffer in the sample cell. ITC data were processed using Origin software (MicroCal), which automatically integrates heat signal and calculates the molar enthalpy change (ΔH_m) and the overall ligand-to-receptor molar ratio ((Taylor, 1970)/[R]) at each injection. ΔH_m was first corrected by subtracting the corresponding blank-titration data. Sigmoidal or near-sigmoidal ΔH_m – [L]/[R] relationships seen in all titrations using ppGpp and GDP were fitted to a single-site model with both ligand-to-Gsk stoichiometry (n) and K_D as variables. The parabolic decay phase of the ADP titration was fitted to a single-site model by fixing the

n = 1.0. The pppGpp titration, when fitted by confining n = 1 or 2, did not give rise to a convergent set of K_D and ΔH_m.

SEC-Multi-Angle Light Scattering (MALS)

SEC was performed using a ÄKTA Pure 25M system equipped with a Superdex-200 increase (10/300) column, which was connected in tandem to a DAWN HELEOS-II multi-angle light scattering (MALS) instrument and OptiLab rEX differential refractometer. Flow-cells of all instruments were set at 25 °C. WT Gsk proteins were purified as His_6-Sumo fusions followed by traceless release of the Sumo tag. The column was equilibrated with degassed HBKT buffer. Gsk protein was freshly refined on the same column and then diluted to 100 μM monomer using HBKT and then treated, or not, with 1 mM ppGpp. 100 μL sample was loaded for each run. Fitting was done with the ASTRA 7.0 software package using the differential refractive index (dRI) signal as the source of concentration, with refractive index increment, dn/dc, set at 0.185 mL/g.

Dynamic Light Scattering (DLS)

DLS was performed in a DynaPro NanoStar Light Scatterer (Wyatt) equilibrated at 30 °C. All Gsk proteins used here were purified as His_6-Sumo fusions followed by traceless release of the Sumo tag. Sample proteins were freshly SEC-refined using HBKT buffer, and diluted in the same buffer (freshly filtered with 0.2-μm membrane) to desired concentrations. 200 μL sample (or HBKT buffer for blank) was applied to a plastic cuvette (Eppendorf Cat# 952010077) for 10 replicates of a 10-second measurement. If relevant, 1 μL 20 mM ppGpp or GDP was mixed with the sample for a final concentration of 100μM, and the measurement was repeated. The correlation function was processed using Dynamics 7.1.2 for estimation of hydrodynamic radii and molecular weight (MwR) of samples using the globular sample model, with dn/dc set at 0.185.

Dimer-tetramer equilibrium of Gsk-ppGpp

In the absence of ppGpp, assuming Gsk exists homogeneously as dimers (Figure 1D, bottom trace). After adding 100 μM ppGpp, Gsk is saturated with ppGpp (K_D = 100 nM, Figure 1B) and has a dynamic equilibrium between dimers and tetramers of Gsk-ppGpp complex. Molecular weight of ppGpp is negligible (1%) compared to Gsk. For solutions containing solutes of the same mass, scattered light intensity is proportional to the weight-average molecular weight (M_w) of solute particles.

$$M_{w,\ -\ ppGpp} = 2M$$

$$M_{w,\ +\ ppGpp} = \frac{(2M)^2[\mathrm{Gsk_2}] + (4M)^2[\mathrm{Gsk_4}]}{2M[\mathrm{Gsk_2}] + 4M[\mathrm{Gsk_4}]}$$

Where M is the molecular weight of Gsk, $[Gsk_2]$ and $[Gsk_4]$ are molarity of dimer and tetramers.

Applying this to 500nM Gsk monomer:

$2[Gsk_2] + 4[Gsk_4] = 500nM$

and from DLS data (Figure. 1E)

$$\frac{M_{w,\ +\ ppGpp}}{M_{w,\ -\ ppGpp}} = 1.67$$

we solved

$$[Gsk_2] = 82nM; [Gsk_4] = 84nM$$

We then calculated the equilibrium constant of Gsk tetramerization:

$$K = [Gsk_4]/[Gsk_2]^2 = 0.0125nM^{-1}$$

and solved for $[Gsk_2]$ and $[Gsk_4]$ for 50, 200, 600, 2000 and 6000 nM Gsk monomer. Percentage of subunit in $[Gsk_2]$ under these conditions were shown as the green curve in Figure 3K.

Limited Factor Xa (FXa) proteolysis

Gsk proteins (WT and FXa-site engineered) were exchanged to a buffer containing 20mM HEPES 7.4, 50 mM KCl, 100 mM NaCl and 2 mM $CaCl_2$ and diluted to 1mg/mL. Guanosine and ppGpp was added from 100mM stock to 2 mM when appropriate. FXa (NEB) was diluted 1+1 in 20mM HEPES 7.4, 150 NaCl and 2 mM $CaCl_2$, and mixed 1+1 to Gsk protein. Final concentrations of Guanosine and ppGpp were 1 mM. Reactions were incubated at 30°C for 40 hrs, then mixed with loading dye free of reducing agent, and resolved on a 4–20% gradient SDS-PAGE. Proteins were visualized using SYPRO-RUBY strain (Invitrogen).

Suppressor isolation and sequencing

The *gsk(K383A)* strain was grown in M9GC liquid medium to stationary phase. 1mL this culture (approximately 1×10^9 CFU) was plated on M9GC+guanosine agar, and the plate was incubated at 30°C for 36hrs. Single colonies were re-streaked on M9GC+guanosine agar, then a single colony from each clone was grown in M9GC liquid medium to OD_{600} = 1.0. Genomic DNA was extracted using DNeasy Blood and Tissue Kit (Qiagen) following standard protocols, and submitted to MIT BioMicro Center for whole-genome sequencing using Miseq (Illumina) with 2×300bp read lengths. Data was mapped to reference genome and normalized using Breseq (Deatherage and Barrick, 2014)

Viability Assays

ML3272 harboring *gsk*(K383A) was grown to OD_{600} = 0.15 in M9GC liquid medium and treated with 2 mM guanosine. 1 mL culture was sampled immediately before guanosine

addition and 80 minutes after, and immediately chilled in ice water. Cells were pelleted and re-suspended in 1mL M9GC without nucleoside. Each sample was then serially diluted to 10^{-6} in 10-fold increments and each dilution was spotted onto M9GC agar plate. Photographs were taken for the plate after overnight incubation at 37 °C.

Quantification of pyrE expression

Cell culture and sampling: *gsk*(WT), *gsk*(K383A) and *gsk*(K383A)*pyrE*$^{++}$ were sampled during their steady-state growth in M9GC without or with inosine or guanosine. Prior to each experiment, each strain was grown overnight in M9GC to stationary phase. The starter cultures were diluted to OD_{600} = 0.01 in fresh M9GC medium and grown at 37 °C. Timing of nucleoside treatment and sampling is listed below. Note that we allowed 120–140 minutes of nucleoside treatment to have cells adapt to the new condition. To ensure sampling each culture at a mid-exponential phase density, nucleosides were added to *gsk*(K383A) at a higher OD_{600} since this strain grows slower after treatment. Note that exponential growth of ML3272 in M9GC with guanosine was interrupted when OD_{600} reached approximately 0.2, likely as a result of a stringent response caused by serine depletion. We thus sampled this culture earlier, before the interruption.

Strain	Nucleoside	OD_{600} when adding the nucleoside	Treatment time (min)	OD_{600} sampling for
gsk(WT) #ML3272	-	0.02	130	0.25–0.30
	inosine	0.02	130	0.25–0.30
	guanosine	0.02	130	0.25–0.30
gsk(K383A) #ML3272	-	-	-	0.25–0.30
	inosine	0.05	140	0.25–0.30
	guanosine	0.15	130	0.25–0.30
gsk(K383A) *pyrE*$^{++}$ #ML3273	-	-	-	0.25–0.30
	inosine	0.02	130	0.25–0.30
	guanosine	0.01	130	0.15–0.18

Quantifying pyrE mRNA by RT-qPCR: For RNA extraction and qPCR, 1 mL of each culture was pipet-mixed with 111 μL stop solution (5% phenol in ethanol). The mixture was then chilled in ice water for 2 minutes and cells pelleted at 20,000 *g* for 2 minutes. RNA was then extracted using Direct-zol RNA Miniprep kit (Zymo Research) following manual protocols. To remove contaminating DNA from RNA preps, 6 μL of Ambion RNA Turbo buffer + 5 μL of Turbo DNase (Invitrogen) were added to each RNA sample (eluted in 50 μL water). After 1-hr incubation at 37 °C, the sample was treated with phenol-chloroform and RNA was ethanol-precipitated from the aqueous phase and re-dissolved in water. Reverse transcription (RT) was performed following standard procedures with 200 ng each RNA sample in 10 μL reaction. Each reaction contained 0.5 μL of 50 ng/μL random hexamers, 0.5 μL of a 10 mM dNTP mix, 1 μL of 10X RT buffer, 2 μL of 25 mM MgCl2, 1 μL of 0.1 M DTT, 1 μL of SUPERase-In (Invitrogen) and 0.5 μL of SuperScript III (Invitrogen). Annealing was performed at 65 °C for 5 minutes, and RT at 50 °C for 1 hour. qRT-PCR

was performed with the Sybr Fast qPCR 2x Master Mix (Kapa). Briefly, ~10 ng of cDNA was incubated with 5 μL of 2x Sybr, 0.6 μL of 5 μM of each primer (G22–1 qPCR1 FP and G22–1 qPCR1 RP, see Table S3), for a final primer concentration of 300 nM, and water to a final volume of 10 μL. Samples were then placed into 384-well white bottom plates, and qRT-PCR done in a LightCycler 480 system (Roche) with the following thermocycling program: 95 °C for 10 minutes, 95 °C for 15 seconds, 60 °C for 30 seconds, and 72 °C for 30 seconds, with 40 cycles of steps 2–4. Data were analyzed by the ddCT method to determine the fold change of each relative to a housekeeping gene (*gyrA*).

Quantifying PyrE protein using In-lysate orotate phosphoribosyltransferase (PRTase) assay: 15 mL of each sample was transferred directly into glass tubes chilled in ice water. Cells were pelleted at 4 °C and the medium aspirated. Each cell pellet was resuspended in a buffer containing 20 mM HEPES-Na 7.4, 50 mM NaCl, 100 μM PMSF, 10 μg/mL lysozyme and 50U/mL benzonase to OD_{600} ~ 15. The suspension was briefly sonicated to lyse. The lysate was cleared at *20000 g* for 5 min and total soluble protein in the supernatant was quantified using BCA assay (Thermo). To determine orotate PRTase activity of each lysate, 100 μL reactions were carried out in a 96-well plate thermostated at 37 °C in a Spectramax M5 plate reader (Molecular Devices). Each reaction contained 50 mM HEPES-Na 7.4, 100 mM KCl, 5 mM $MgCl_2$, 1 mM TCEP, 1 mM pRpp, 0.5 mM orotate and 50 μL ML3271 or ML3272 cleared lysate or 20 μL ML3273 cleared lysate. PRTase activity was quantified as the velocity of absorbance loss at 296nm normalized by total soluble protein (Schwartz and Neuhard, 1975).

Biochemical Activity Assays

General considerations: All Gsk and GuaB proteins used here were purified as His_6-Sumo fusions followed by traceless release of the Sumo tag. Unless noted otherwise, reactions were performed at 100-μL scale in 96-well plates at 30 °C in a Spectramax M5 plate reader (Molecular Devices). Absorbance of each reaction was monitored for the absorbance at 340 nm (A340) every 30 seconds. Water-soluble small-molecule reagents were dissolved in water and pH adjusted to 7.4. Reagent-grade GDP contains a substantial amount of GMP, a GuaB inhibitor, and thus had to be purified over a Mono Q column prior to use. Guanosine was dissolved by adding 1 equivalence of NaOH. All above chemicals were diluted to 10X working concentration in water immediately prior to use. To couple ADP formation to NADH consumption, a 10X pyruvate kinase-lactose dehydrogenase (PK-LDH) mixture was prepared in water, which contained PEP (monopotassium salt from Roche, 37.5 mM), NADH (disodium salt from Roche, 7.5 mM), PK and LDH (100 units/mL each) (Norby, 1988). Typically, a reaction was assembled by first mixing all components except one essential substrate. After pre-incubating the plate at 30 °C for 5 minutes, the mixture was then transferred to the left-out substrate using a multi-channel pipette at $t = 0$ to initiate the reaction. Activity was quantified as the initial velocity of absorbance loss or gain at 340nm.

IMP-dehydrogenase (GuaB) assay: GuaB catalyzes the oxidization of IMP into xanthosine monophosphate (XMP) and the concomitant production of NADH from NAD^+:

$$IMP + NAD^+ \rightarrow XMP + NADH$$

In assays done in the presence of Mg^{2+}, each reaction contained 40 mM HEPES-Na pH 7.4, 150 mM KCl, 5 mM $MgCl_2$, 1 mM TCEP, 100 μM IMP, 2 mM NAD+, 300 nM *E. coli* GuaB and indicated amounts GMP or ppGpp-Mg. For the Mg^{2+}-free assay, $MgCl_2$ was excluded from the reaction buffer, and ppGpp lithium salt was used in place of the ppGpp-Mg complex. Volume of each reaction was 200uL due to the limited amount of IMP substrate.

Inosine kinase (Gsk) assay coupled to GuaB activity: Because pyruvate kinase phosphorylates GDP with PEP, an alternative strategy was required to test the effect of GDP on Gsk activity. GuaB coupled IMP production to the production of NADH. The overall reaction was:

$$Inosine + ATP + NAD^+ \rightarrow XMP + ADP + NADH + H^+$$

Each reaction contained 40 mM HEPES-Na pH 7.4, 150 mM KCl, 5 mM $MgCl_2$, 1 mM TCEP, 1 mM inosine, 5 mM ATP-Mg, 5 mM NAD+, 3 μM IMPΔH, 50 nM Gsk or Gsk(K383A), and indicated amounts of ppGpp-Mg or GDP.

Inosine/guanosine kinase (Gsk) assay coupled to PK-LDH activity: PK-LDH coupled ADP production to the consumption of NADH. The overall reaction was: Inosine(Guanosine) + PEP + NADH + H^+ → IMP(GMP) + lactate + NAD^+ Each reaction contained 40 mM HEPES-Na pH 7.4, 150 mM KCl, 5 mM $MgCl_2$, 1 mM TCEP, 1X PK-LDH mixture. Default concentrations of other ingredients are 50nM Gsk or variants, 5 mM ATP-Mg, 1 mM inosine or guanosine, unless indicated otherwise in figure legends.

Glutamine amidophosphoribosyltransferase (PurF) assay: PurF catalyzes the production of 5-phosphoriboylamine (PRA) from pRpp and glutamine. The reaction was coupled to the PRA-glycine ligase activity of excess recombinant *E. coli* PurD (Wang et al., 2019), which hydrolyzes ATP to produce glycinamide-ribonucleotide (GAR) from 5-PRA and glycine. PK-LDH then coupled ADP production to the consumption of NADH. The overall reaction was:

$$glutamine + pRpp + glycine + H_2O + PEP + NADH + H^+ \rightarrow glutamate + GAR + PPi + Pi + lactate + NAD^+$$

Each reaction contained 50 mM HEPES-Na pH 7.4, 150 mM NaCl, 10 mM $MgCl_2$, 1 mM TCEP, 1 mM pRpp-Mg, 5 mM glutamine, 5 mM ATP, 5 mM glycine, 1 μM *E. coli* PurD, 1X PK-LDH mixture and indicated amounts ppGpp-Mg. Final concentrations for PurF were 50 nM and 1 μM for *E. coli* and *B. subtilis* homologs, respectively.

Adenylosuccinate synthase (PurA) assay: PurA ligates asparate to IMP to form adenylosuccinate. The reaction was coupled to the hydrolysis of GTP. GDP produced was then phosphorylated by ATP with excess recombinant *E. coli* Ndk (Wang et al., 2019), and the concomitant formation of ADP was coupled to NADH consumption by PK-LDH. The overall reaction was:

$$\text{IMP} + \text{aspartate} + \text{PEP} + \text{NADH} + \text{H}^+ \rightarrow \text{adenylosuccinate} + \text{Pi} + \text{lactate} + \text{NAD}^+$$

Each reaction contained 50 mM HEPES-Na pH 7.4, 150 mM NaCl, 10 mM $MgCl_2$, 1 mM TCEP, 10 mM L-aspartate, 2 mM IMP, 2 mM ATP, 300 nM PurA, 1 μM *E. coli* Ndk, 1X PK-LDH mixture and indicated amounts of GTP-Mg and/or ppGpp-Mg.

Metabolic Profiling

Inosine treatment of guaB$^{\Delta CBS}$ with or without ppGpp induction: *guaB*$^{\Delta CBS}$ strains ML2922 (+ pRelÅ) and ML2923 (+ pRelÅ(D275G)) were grown in M9-glucose (M9G) medium and treated with 10 mM inosine alone or 10 mM inosine plus 30 μM IPTG when OD_{600} reached 0.3. Pre-treatment cultures were sampled 1 minute before treatment. Post-treatment culture was sampled at indicated time points.

Steady-state growth of gsk(K383A) (ML3272) and gsk(K383A)pyrE^{++} (ML3273) with or without purine nucleosides: See "Quantification of *pyrE* mRNA and PyrE protein levels" for procedures of bacterial culture and nucleoside treatment.

Amino acid downshift of gsk(K383A) and gsk(WT): Prior to each experiment, strains were grown overnight in M9GC supplemented with inosine and uridine (M9GCIU) to stationary phase and diluted to OD_{600} = 0.01 in the same medium. The starter culture was diluted into 120 mL M9GCIU containing 0.5% (w/v) casamino acids to OD_{600} = 0.01 and grown at 37 °C. The destination medium, M9G supplemented with inosine and uridine (M9GIU), was pre-heated to 37 °C. When OD_{600} reached between 0.25 and 0.35, cells from each culture was vacuum-collected on a 90-mm hydrophilic PVDF membrane (0.22 μm pore size). After the starting medium drained (t = 0), the membrane was quickly washed with 2 × 10 mL pre-warmed M9GIU, re-suspended, and then transferred in 2 × 10mL M9GIU to make ~80 mL culture in the destination medium. Pre-downshift culture was sampled 2 minutes before filter-collecting the culture. Post-downshift culture was sampled at indicated time points.

Downshift experiments were also performed at smaller scales to record growth recovery and to measure (p)ppGpp levels at a time point after growth recovers. These cultures were prepared at 15-mL scale in M9GCIU and grown to OD_{600} around 0.20 before cells were collected on a 25-mm hydrophilic PVDF membrane (0.22 μm pore size). 1 mL M9GCIU culture was also saved in a glass tube chilled in an ice-water batch for OD_{600} measurement (OD_{M9GCIU}). The membrane was washed with 3 mL pre-warmed destination medium and then transferred to a flask containing 12 mL destination medium. Cells spontaneously disperse in the new medium within a few minutes. OD_{600} immediately after downshift (OD_0, t = 0 data points in Figure 5F) was calculated as: $OD_0 = OD_{M9GCIU} * V_{M9GCIU} / 12$

mL. The post-downshift culture was sampled when OD_{600} reached between 2.5 and 4 times of OD_0, ranging from 0.5–0.9 for (p)ppGpp quantification. Cells downshifted to M9GIU containing histidine and tryptophan were also sampled at t = 60 min and t = 120 min for quantification of other purine nucleotides. Note, that to calculate post-downshift generation times, we performed regression on the semi-log growth curve for linear segments typically occurring between 2.5 times OD_0 and 2.5. At least three points from each growth curve were used for regression. Generation time, t_{gen} was calculated from the slope, k by $t_{gen} = \ln 2 / k$.

Extraction of hydrophilic metabolites: Experimental procedures for metabolite extraction for analysis using hydrophilic chromatography in tandem with mass spectrometry (pHILIC-MS) or anion-exchange chromatography were modified from those described by previously (Park et al., 2016). Briefly, *E. coli* cells were collected on a 0.22-μm hydrophilic PVDF membrane by vacuum filtration and washed briefly with 160 mM NaCl. At the same time, the culture was sampled for OD_{600} measurements. Cells on the membrane were subsequently immersed in ice-cold lysis solvent, a methanol-acetonitrile-water mixture in a volume ratio of 40:40:20 containing 0.05% (v/v) Metabolomics Amino Acid Mix Standard solution (Cambridge Isotope Laboratories, MSK-A2–1.2) as the internal standard (ISTD). Lysates were briefly sonicated and, after removal of PVDF membranes, diluted by the lysis solvent for a uniform cell density, typically 1.0 OD_{600} cells per mL solvent.

Nucleotide quantification using anion exchange chromatography: Lysate equivalent to 1.0 OD_{600} cells was transferred to 3.0 mL aqueous solution of 10 mM Tris-HCl pH 8.0. Insoluble material was pelleted at 10,000 *g*, and the supernatant was applied to a Mono Q 5/50 column (GE Healthcare) after passing through a 0.22-μm syringe filter. Bound metabolites were eluted at 4 °C using a linear gradient of buffer A (5 mM Tris-HCl pH 8.0) and buffer B (5 mM Tris-HCl pH 8.0, 1M NaCl), with the percentage of buffer B increasing from 0 to 35% within 20 mL. Absorbance chromatograms recorded at 254 nm were integrated and peaks for ADP (12.8 mL, elution volume after gradient begins), ATP (15.1 mL), GTP (16.2 mL), ppGpp (18.5 mL) and pppGpp (19.7 mL) were quantified using Unicorn Evaluation module (version 6.4 or 7.0), using extinction coefficient $\varepsilon = 15000 M^{-1} \cdot cm^{-1}$ for ATP and $\varepsilon = 13000 M^{-1} \cdot cm^{-1}$ for GTP, ppGpp or pppGpp. Note that we only used anion exchange to quantify ADP, ATP and GTP for "+His/Trp" data in Figures 5I and Fig. S5D. All other quantification of these three nucleotides was based on pHILIC-MS data.

Polar metabolite profiling by pHILIC-MS: For pHILIC-MS, lysates corresponding to 1.0 OD_{600} cells were first cleared at 10,000 *g*, and the supernatant was subsequently lyophilized. Dried polar samples were resuspended in 100 μL water and 2 μL was injected into a ZIC-pHILIC 150 × 2.1 mm (5 μm particle size) column (EMD Millipore). Analysis was conducted on a QExactive benchtop orbitrap mass spectrometer equipped with an Ion Max source and a HESI II probe, which was coupled to a Dionex UltiMate 3000 UPLC system (Thermo Fisher Scientific, San Jose, CA). External mass calibration was performed using the standard calibration mixture every 7 days. Chromatographic separation was achieved using the following conditions: Buffer A was 20 mM ammonium carbonate, 0.1% ammonium hydroxide; buffer B was acetonitrile. The column oven and autosampler

tray were held at 25 °C and 4 °C, respectively. The chromatographic gradient was run at a flow rate of 0.150 ml/min as follows: 0–20 min.: linear gradient from 80% to 20% B; 20–20.5 min.: linear gradient from 20% to 80% B; 20.5–28 min.: hold at 80% B. The mass spectrometer was operated in full-scan, polarity switching mode with the spray voltage set to 3.0 kV, the heated capillary held at 275 °C, and the HESI probe held at 350 °C. The sheath gas flow was set to 40 units, the auxiliary gas flow was set to 15 units, and the sweep gas flow was set to 1 unit. The MS data acquisition was performed in a range of 70–1000 m/z, with the resolution set at 70,000, the AGC target at 10^{-6}, and the maximum injection time at 20 msec. Relative quantitation of polar metabolites was performed with XCalibur QuanBrowser 2.2 (Thermo Fisher Scientific) using a 5 ppm mass tolerance and referencing an in-house library of chemical standards.

For relative quantifications, a peak area of 5×10^3 was arbitrarily assigned to undetected metabolites. Then, peak area of each metabolite was normalized to the internal standard amino acid with the closest retention time and ionized by the same charge. Fold change of metabolite levels between conditions were then calculated based on normalized peak areas.

For absolute quantifications, standard samples containing AMP, ADP, ATP, GMP, GDP, and GTP at a series of known concentrations were prepared in water containing 0.5% (v/v) internal standard and 2 μL was analyzed under the same conditions. Note that this internal standard concentration was identical to that in metabolome samples. Peak areas of all 6 purine nucleotides were therefore normalized to that of $^{13}C_6{}^{15}N$-glutamate, and standard curves were generated. Absolute levels of the above nucleotides in *E. coli* samples were then derived through interpolation.

QUANTIFICATION AND STATISTICAL ANALYSIS

Basic quantifications:

proteins are quantified in-solution based on absorbance at 280nm using the extinction coefficient provided by the Protparam tool (Wilkins et al., 1999). DNA and RNA are quantified based on $\varepsilon = 20(mg/mL)^{-1}\bullet cm^{-1}$ for DNA and $\varepsilon = 25(mg/mL)^{-1}\bullet cm^{-1}$ for RNA. Before serving as titrants in ITC, inhibitors in biochemical assays or external standards in LC-MS, adenosine and guanosine nucleotides were quantified based on absorbance at 260nm ($\varepsilon = 15400M^1cm^{-1}$) and 251nm ($\varepsilon = 13700M^{-1}\bullet cm^{-1}$), respectively. Reagents used otherwise were quantified by weight before solution preparation.

Other quantifications:

Quantifications of RNA by qRT-PCR, initial velocities of chromogenic biochemical assays, metabolites by LC-MS, and fitting of ITC, SEC-MALS and DLS data were addressed in respective sections in METHOD DETAILS.

Statistical details:

in this study, we use small number of replications (typically 2–4) in all experiments because experimental error is much smaller compared to differences between quantification results from which our conclusions were drawn. We replicate cell-culture experiments using

separate starter cultures in different flasks or multiplex plate wells. For growth curves, we show one representative for each condition. For quantification of cellular contents using RT-qPCR, anion-exchange chromatography or LC-MS, we present bargraphs or time courses showing results from each replicate. We replicate each DLS experiment with fresh protein samples from at least two different batches. We replicate biochemical-activity assays by assembling the reactions using the same set of recombinant protein and stock solutions (technical replicate). Results from each replicate were also marked in related bargraphs or plots.

We performed Student's *t* test for Figures 5G–H using Prism 7 (GraphPad). We did not assume equal dispersion of datasets in each pairwise test. π-value threshold was set to a conventional value of 0.05.

Supplementary Material

Refer to Web version on PubMed Central for supplementary material.

Acknowledgements

This work was supported by fellowships from the Jane Coffin Childs Memorial Fund for Medical Research and the NIH (K99GM135536) to B.W. and an NIH grant to M.T.L. (R01GM082899), who is also an Investigator of the Howard Hughes Medical Institute.

This research made use of the Pilatus detector (RR029205) at the NE-CAT beamline 24-IDC (GM103403) of the Advanced Photon Source (DE-AC02–06CH11357). We thank the Whitehead Institute Metabolite Profiling Core Facility for measuring metabolite levels. Instrumentation resources from the Biophysical Instrumentation Facility for the Study of Complex Macromolecular Systems (NSF-0070319), the Structural Biology Core Facility, and the BioMicro Center in the Department of Biology at MIT are gratefully acknowledged.

References

Adams PD, Afonine PV, Bunkoczi G, Chen VB, Davis IW, Echols N, Headd JJ, Hung LW, Kapral GJ, Grosse-Kunstleve RW, et al. (2010). PHENIX: a comprehensive Python-based system for macromolecular structure solution. Acta crystallographica Section D, Biological crystallography 66, 213–221. [PubMed: 20124702]

Anderson BW, Hao A, Satyshur KA, Keck JL, and Wang JD (2020). Molecular mechanism of regulation of the purine salvage enzyme XPRT by the alarmones pppGpp, ppGpp, and pGpp. bioRxiv, 2020.2003.2004.977603.

Anderson BW, Liu KQ, Wolak C, Dubiel K, She FK, Satyshur KA, Keck JL, and Wang JD (2019). Evolution of (p)ppGpp-HPRT regulation through diversification of an allosteric oligomeric interaction. Elife 8.

Atkinson GC, Tenson T, and Hauryliuk V. (2011). The RelA/SpoT Homolog (RSH) Superfamily: Distribution and Functional Evolution of ppGpp Synthetases and Hydrolases across the Tree of Life. Plos One6.

Baba T, Ara T, Hasegawa M, Takai Y, Okumura Y, Baba M, Datsenko KA, Tomita M, Wanner BL, and Mori H. (2006). Construction of Escherichia coli K-12 in-frame, single-gene knockout mutants: the Keio collection. Molecular systems biology2, 2006 0008.

Bonekamp F, Clemmesen K, Karlstrom O, and Jensen KF (1984). Mechanism of Utp-Modulated Attenuation at the Pyre Gene of Escherichia-Coli - an Example of Operon Polarity Control through the Coupling of Translation to Transcription. Embo J 3, 2857–2861. [PubMed: 6098450]

Buglino J, Shen V, Hakimian P, and Lima CD (2002). Structural and biochemical analysis of the Obg GTP binding protein. Structure 10, 1581–1592. [PubMed: 12429099]

Cashel M, and Gallant J. (1969). Two compounds implicated in the function of the RC gene of Escherichia coli. Nature221, 838–841. [PubMed: 4885263]

Chen S, Tomchick DR, Wolle D, Hu P, Smith JL, Switzer RL, and Zalkin H. (1997). Mechanism of the synergistic end-product regulation of Bacillus subtilis glutamine phosphoribosylpyrophosphate amidotransferase by nucleotides. Biochemistry36, 10718–10726. [PubMed: 9271502]

Cherepanov PP, and Wackernagel W. (1995). Gene disruption in Escherichia coli: TcR and KmR cassettes with the option of Flp-catalyzed excision of the antibiotic-resistance determinant. Gene158, 9–14. [PubMed: 7789817]

Dalebroux ZD, and Swanson MS (2012). ppGpp: magic beyond RNA polymerase. Nat Rev Microbiol 10, 203–212. [PubMed: 22337166]

Datsenko KA, and Wanner BL (2000). One-step inactivation of chromosomal genes in Escherichia coli K-12 using PCR products. Proceedings of the National Academy of Sciences of the United States of America 97, 6640–6645. [PubMed: 10829079]

Deatherage DE, and Barrick JE (2014). Identification of Mutations in Laboratory-Evolved Microbes from Next-Generation Sequencing Data Using breseq. Methods Mol Biol 1151, 165–188. [PubMed: 24838886]

Emsley P, Lohkamp B, Scott WG, and Cowtan K. (2010). Features and development of Coot. Acta crystallographica Section D, Biological crystallography66, 486–501. [PubMed: 20383002]

Fan H, Hahm J, Diggs S, Perry JJ, and Blaha G. (2015). Structural and Functional Analysis of BipA, a Regulator of Virulence in Enteropathogenic Escherichia coli. The Journal of biological chemistry290, 20856–20864. [PubMed: 26163516]

Gallant J, Irr J, and Cashel M. (1971). The mechanism of amino acid control of guanylate and adenylate biosynthesis. The Journal of biological chemistry246, 5812–5816. [PubMed: 4938039]

Gibson DG, Young L, Chuang RY, Venter JC, Hutchison CA 3rd, and Smith HO (2009). Enzymatic assembly of DNA molecules up to several hundred kilobases. Nature methods 6, 343–345. [PubMed: 19363495]

Hara A, and Sy J. (1983). Guanosine 5'-triphosphate, 3'-diphosphate 5'-phosphohydrolase. Purification and substrate specificity. The Journal of biological chemistry258, 1678–1683. [PubMed: 6130093]

Harms A, Maisonneuve E, and Gerdes K. (2016). Mechanisms of bacterial persistence during stress and antibiotic exposure. Science354.

Haseltine WA, and Block R. (1973). Synthesis of guanosine tetra- and pentaphosphate requires the presence of a codon-specific, uncharged transfer ribonucleic acid in the acceptor site of ribosomes. Proc Natl Acad Sci U S A70, 1564–1568. [PubMed: 4576025]

Hauryliuk V, Atkinson GC, Murakami KS, Tenson T, and Gerdes K. (2015). Recent functional insights into the role of (p)ppGpp in bacterial physiology. Nat Rev Microbiol13, 298–309. [PubMed: 25853779]

Hochstadt-Ozer J, and Cashel M. (1972). The regulation of purine utilization in bacteria. V. Inhibition of purine phosphoribosyltransferase activities and purine uptake in isolated membrane vesicles by guanosine tetraphosphate. The Journal of biological chemistry247, 7067–7072. [PubMed: 4343167]

Holm L, and Laakso LM (2016). Dali server update. Nucleic acids research 44, W351–355. [PubMed: 27131377]

Hove-Jensen B, Andersen KR, Kilstrup M, Martinussen J, Switzer RL, and Willemoes M. (2017). Phosphoribosyl Diphosphate (PRPP): Biosynthesis, Enzymology, Utilization, and Metabolic Significance. Microbiology and molecular biology reviews : MMBR81.

Hove-Jensen B, Harlow KW, King CJ, and Switzer RL (1986). Phosphoribosylpyrophosphate synthetase of Escherichia coli. Properties of the purified enzyme and primary structure of the prs gene. The Journal of biological chemistry 261, 6765–6771. [PubMed: 3009477]

Jensen KF (1979). Apparent Involvement of Purines in the Control of Expression of Salmonella-Typhimurium-Pyr Genes - Analysis of a Leaky Guab Mutant Resistant to Pyrimidine Analogs. J Bacteriol 138, 731–738. [PubMed: 378934]

Jensen KF, Dandanell G, Hove-Jensen B, and Willemoes M. (2008). Nucleotides, Nucleosides, and Nucleobases. EcoSal Plus3.

Kabsch W. (2010). Xds. Acta crystallographica Section D, Biological crystallography66, 125–132. [PubMed: 20124692]

Kanjee U, Ogata K, and Houry WA (2012). Direct binding targets of the stringent response alarmone (p)ppGpp. Mol Microbiol 85, 1029–1043. [PubMed: 22812515]

Kawasaki H, Shimaoka M, Usuda Y, and Utagawa T. (2000). End-product regulation and kinetic mechanism of guanosine-inosine kinase from Escherichia coli. Bioscience, biotechnology, and biochemistry64, 972–979.

Krasny L, and Gourse RL (2004). An alternative strategy for bacterial ribosome synthesis: Bacillus subtilis rRNA transcription regulation. Embo J 23, 4473–4483. [PubMed: 15496987]

Kriel A, Bittner AN, Kim SH, Liu KQ, Tehranchi AK, Zou WY, Rendon S, Chen R, Tu BP, and Wang JD (2012). Direct Regulation of GTP Homeostasis by (p)ppGpp: A Critical Component of Viability and Stress Resistance. Mol Cell 48, 231–241. [PubMed: 22981860]

Krissinel E, and Henrick K. (2007). Inference of macromolecular assemblies from crystalline state. J Mol Biol372, 774–797. [PubMed: 17681537]

Langmead B, and Salzberg SL (2012). Fast gapped-read alignment with Bowtie 2. Nature methods 9, 357–359. [PubMed: 22388286]

Liu KQ, Bittner AN, and Wang JD (2015). Diversity in (p)ppGpp metabolism and effectors. Curr Opin Microbiol 24, 72–79. [PubMed: 25636134]

McCoy AJ, Grosse-Kunstleve RW, Adams PD, Winn MD, Storoni LC, and Read RJ (2007). Phaser crystallographic software. Journal of applied crystallography 40, 658–674. [PubMed: 19461840]

Mori H, Iida A, Teshiba S, and Fujio T. (1995). Cloning of a guanosine-inosine kinase gene of Escherichia coli and characterization of the purified gene product. J Bacteriol177, 4921–4926. [PubMed: 7665468]

Norby JG (1988). Coupled assay of Na+,K+-ATPase activity. Methods in enzymology 156, 116–119. [PubMed: 2835597]

Otwinowski Z, and Minor W. (1997). Processing of X-ray diffraction data collected in oscillation mode. Methods in enzymology276, 307–326.

Park J, and Gupta RS (2008). Adenosine kinase and ribokinase--the RK family of proteins. Cell Mol Life Sci 65, 2875–2896. [PubMed: 18560757]

Park JO, Rubin SA, Xu YF, Amador-Noguez D, Fan J, Shlomi T, and Rabinowitz JD (2016). Metabolite concentrations, fluxes and free energies imply efficient enzyme usage. Nature chemical biology 12, 482–489. [PubMed: 27159581]

Pausch P, Steinchen W, Wieland M, Klaus T, Freibert SA, Altegoer F, Wilson DN, and Bange G. (2018). Structural basis for (p)ppGpp-mediated inhibition of the GTPase RbgA. The Journal of biological chemistry293, 19699–19709. [PubMed: 30366986]

Petersen C. (1999). Inhibition of cellular growth by increased guanine nucleotide pools. Characterization of an Escherichia coli mutant with a guanosine kinase that is insensitive to feedback inhibition by GTP. The Journal of biological chemistry274, 5348–5356. [PubMed: 10026143]

Pimkin M, and Markham GD (2008). The CBS subdomain of inosine 5'-monophosphate dehydrogenase regulates purine nucleotide turnover. Molecular microbiology 68, 342–359. [PubMed: 18312263]

Pimkin M, Pimkina J, and Markham GD (2009a). A Regulatory Role of the Bateman Domain of IMP Dehydrogenase in Adenylate Nucleotide Biosynthesis. Journal of Biological Chemistry 284, 7960–7969.

Pimkin M, Pimkina J, and Markham GD (2009b). A regulatory role of the Bateman domain of IMP dehydrogenase in adenylate nucleotide biosynthesis. The Journal of biological chemistry 284, 7960–7969. [PubMed: 19153081]

Potrykus K, and Cashel M. (2008). (p)ppGpp: Still Magical?Annu Rev Microbiol62, 35–51. [PubMed: 18454629]

Potrykus K, Murphy H, Philippe N, and Cashel M. (2011). ppGpp is the major source of growth rate control in E. coli. Environmental microbiology13, 563–575. [PubMed: 20946586]

Ratnayake-Lecamwasam M, Serror P, Wong KW, and Sonenshein AL (2001). Bacillus subtilis CodY represses early-stationary-phase genes by sensing GTP levels. Genes Dev 15, 1093–1103. [PubMed: 11331605]

Ross W, Sanchez-Vazquez P, Chen AY, Lee JH, Burgos HL, and Gourse RL (2016). ppGpp Binding to a Site at the RNAP-DksA Interface Accounts for Its Dramatic Effects on Transcription Initiation during the Stringent Response. Mol Cell 62, 811–823. [PubMed: 27237053]

Sanchez-Vazquez P, Dewey CN, Kitten N, Ross W, and Gourse RL (2019). Genome-wide effects on Escherichia coli transcription from ppGpp binding to its two sites on RNA polymerase. Proc Natl Acad Sci U S A 116, 8310–8319. [PubMed: 30971496]

Schreiber G, Metzger S, Aizenman E, Roza S, Cashel M, and Glaser G. (1991). Overexpression of the relA gene in Escherichia coli. The Journal of biological chemistry266, 3760–3767. [PubMed: 1899866]

Schumacher MA, Scott DM, Mathews II, Ealick SE, Roos DS, Ullman B, and Brennan RG (2000). Crystal structures of Toxoplasma gondii adenosine kinase reveal a novel catalytic mechanism and prodrug binding. J Mol Biol 296, 549–567. [PubMed: 10669608]

Schwartz M, and Neuhard J. (1975). Control of expression of the pyr genes in Salmonella typhimurium: effects of variations in uridine and cytidine nucleotide pools. J Bacteriol121, 814–822. [PubMed: 163814]

Steinchen W, and Bange G. (2016). The magic dance of the alarmones (p)ppGpp. Mol Microbiol101, 531–544. [PubMed: 27149325]

Wang B, Dai P, Ding D, Del Rosario A, Grant RA, Pentelute BL, and Laub MT (2019). Affinity-based capture and identification of protein effectors of the growth regulator ppGpp. Nature chemical biology 15, 141–150. [PubMed: 30559427]

Wang B, Zhao A, Novick RP, and Muir TW (2015). Key driving forces in the biosynthesis of autoinducing peptides required for staphylococcal virulence. Proceedings of the National Academy of Sciences of the United States of America 112, 10679–10684. [PubMed: 26261307]

Wilkins MR, Gasteiger E, Bairoch A, Sanchez JC, Williams KL, Appel RD, and Hochstrasser DF (1999). Protein identification and analysis tools in the ExPASy server. Methods Mol Biol 112, 531–552. [PubMed: 10027275]

Zhang Y, Zbornikova E, Rejman D, and Gerdes K. (2018). Novel (p)ppGpp Binding and Metabolizing Proteins of Escherichia coli. mBio9.

Zhang YE, Baerentsen RL, Fuhrer T, Sauer U, Gerdes K, and Brodersen DE (2019). (p)ppGpp Regulates a Bacterial Nucleosidase by an Allosteric Two-Domain Switch. Mol Cell 74, 1239–1249 e1234. [PubMed: 31023582]

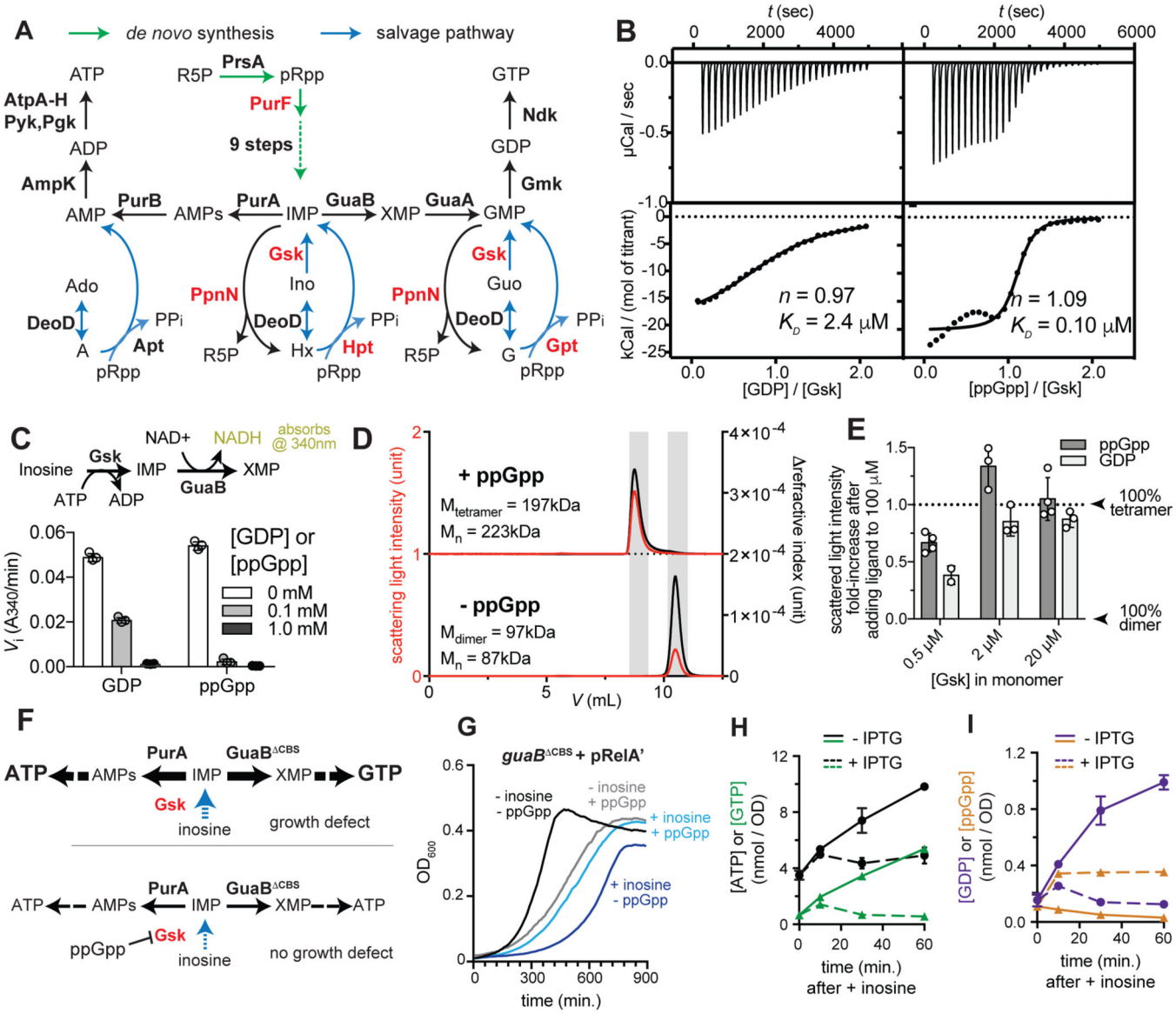

Figure 1. ppGpp and GDP bind to and inhibit Gsk

(A) Summary of *de novo* synthesis and salvage pathways for purine nucleotides. Enzymes shown in red are direct targets of ppGpp in *E. coli*.

(B) ITC traces (top) and fitted isotherms (bottom) for the titration of 10 μM Gsk monomer with 100 μM GDP (left) or ppGpp (right). K_D, dissociation constant; *n*, ligand-Gsk stoichiometry. See Table S1 for binding enthalpy and fitting errors.

(C) Inosine kinase activity of Gsk in the presence of indicated concentration of GDP or ppGpp. Activity was measured by coupling IMP production to NADH formation (scheme on top).

(D) SEC-MALS analysis of Gsk with or without ppGpp in the running buffer: M_n, number-average molecular weight (MW) fitted for the shadowed segment.

(E) Fold increase of scattered light intensity of Gsk at indicated concentrations after adding 100 μM GDP or ppGpp.

(F) Schematic indicating that cells producing GuaB$^{\Delta CBS}$ show uncontrolled purine nucleotide salvage with inosine in the growth medium converted into IMP, via Gsk (top). The resulting growth defect is suppressed by a deletion of *gsk* (Pimkin et al., 2009b) or by expressing ppGpp.

(G) Growth curves for *guaB*$^{\Delta CBS}$ cells harboring the pRelÅ plasmid and grown with or without 10 mM inosine in the medium and with or without 30 μM IPTG to induce, or not, ppGpp production. For each condition, one representative curve of three replicates is shown.

(H-I) Levels of ATP and GTP (H) or GDP and ppGpp (I) in the *guaB*$^{\Delta CBS}$ + pRelÅ strain following addition of inosine and either with or without IPTG to induce ppGpp production, as indicated. Error bars indicate range from two separate cultures.

See also Figure S1.

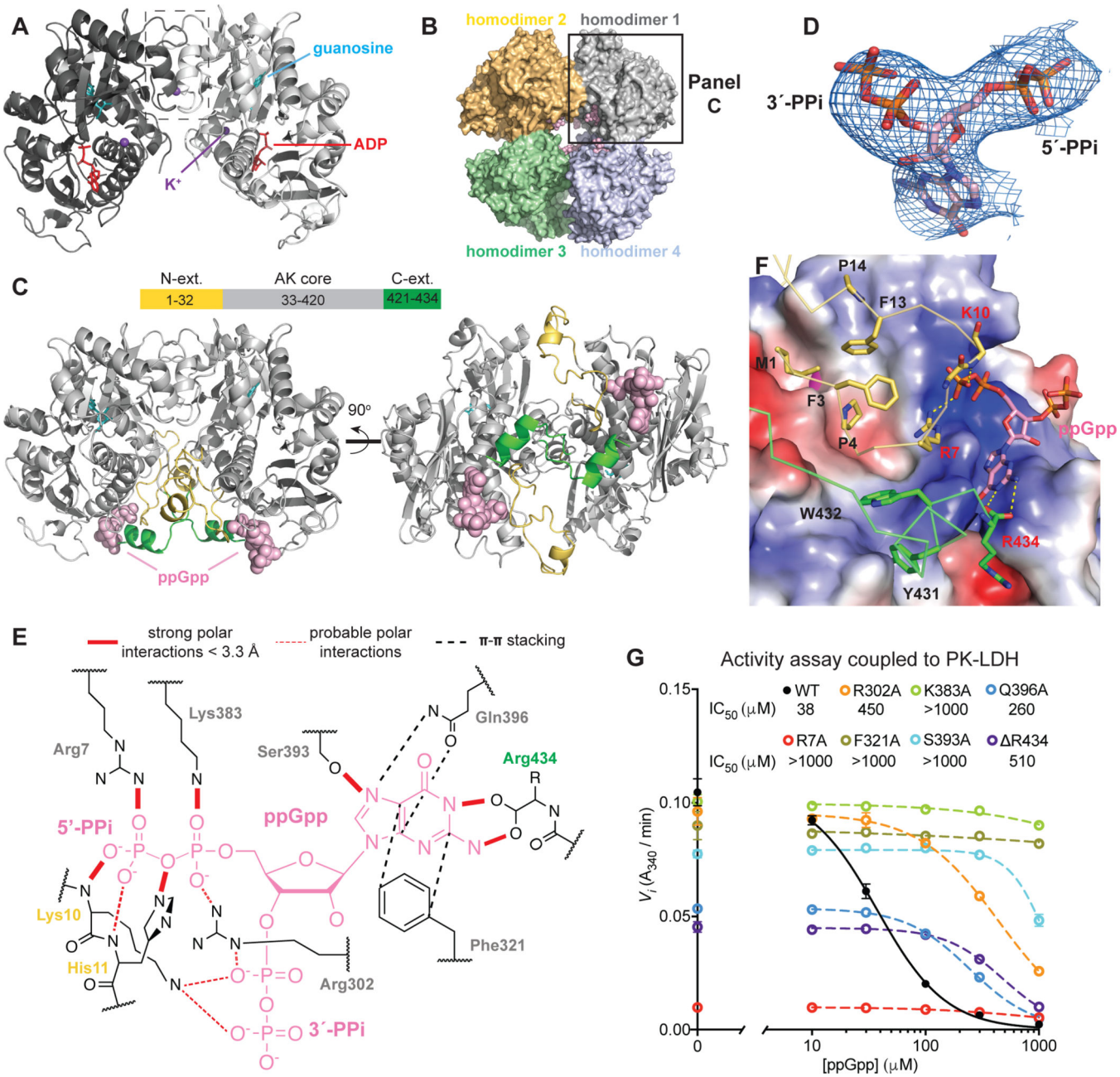

Figure 2. Gsk accommodates ppGpp by re-structuring its terminal sequences

(A) Cartoon of Gsk homodimer in complex with guanosine and ADP. Dashed box indicates dimer interface detailed in Figure S2B–C.

(B-C) Crystallographic asymmetric unit (B) and a Gsk homodimer (C) in ppGpp-bound conformations, with a scheme showing domain architecture of Gsk above in panel (C).

(D) Overlay of the ppGpp stick model with the 2Fo-Fc density map in blue mesh contoured at 1s. (E) 2D map of molecular recognition between ppGpp and Gsk.

(F) ppGpp recognition by terminal extensions. Yellow dashes indicate probable electrostatic or hydrogen bonding (<3.3 Å between heavy atoms). Black and red characters indicate

residues providing hydrophobic packing or specific recognition of ppGpp. The AK core is shown as an electrostatic potential surface.

(G) Inosine kinase activity of indicated Gsk variants as a function of ppGpp concentration fitted to an inhibition model derived from Hill equation. Error bars show S.D. of three separate reactions. See also Figure S2.

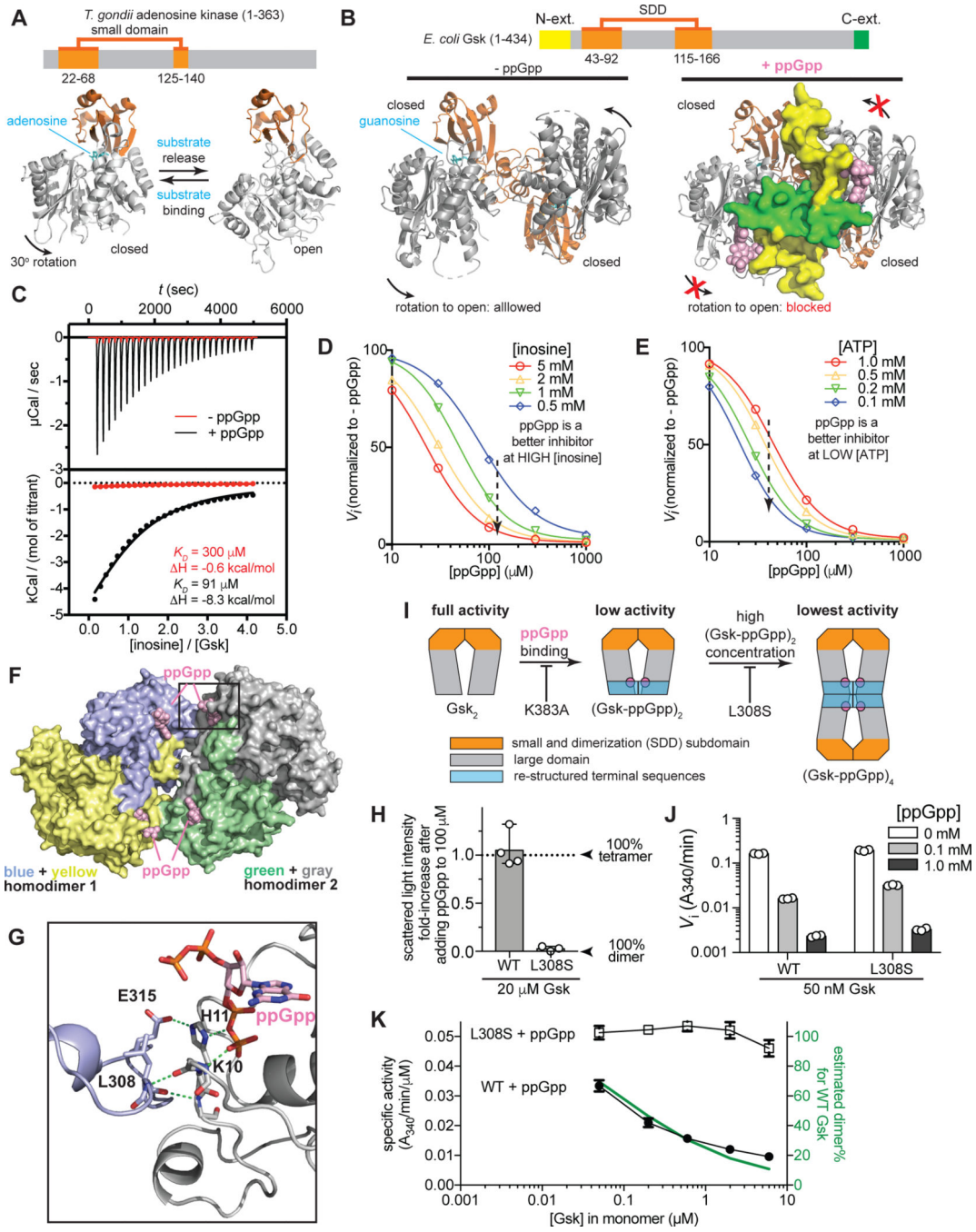

Figure 3. ppGpp inhibits Gsk by blocking the enzyme from accessing the open conformation and promoting tetramerization

(A) Structural rearrangement of *T. gondii* adenosine kinase (AK) from closed (left, PDB ID: 1LII) to open (right, PDB ID: 1LIO) conformations. Nucleoside substrate (adenosine) is shown as cyan sticks.

(B) ppGpp-free (left) and ppGpp-bound (right) Gsk homodimers are positioned with one subunit aligned to the closed *T. gondii* AK in (A). Terminal extension sequences re-structured following ppGpp binding are highlighted as Van der Waals surfaces, which blocks the movement required for opening the nucleoside binding cleft.

(C) ITC traces (top) and fitted isotherms (bottom) for the titration of 100 μM Gsk monomer using 2 mM inosine. Buffer for Gsk and inosine either contains (black), or not (red), free ppGpp at 200 μM. See Table S1 for binding enthalpy and fitting errors.
(D-E) Inosine kinase activity of Gsk as a function of ppGpp concentration with (D) 5 mM ATP-Mg and indicated concentrations of inosine; or (E) 1mM inosine and indicated concentration of ATP-Mg.
(F) Overview of the tetrameric assembly of Gsk driven by ppGpp. Each subunit has a different color. Black box indicates one of two copies of interface highlighted in panel (G).
(G) Zoom-in view of the hydrogen-bonding network across Gsk homodimers. Green dashes indicate probable electrostatic or hydrogen bonding (<3.3 Å between heavy atoms).
(H) Fold increase of scattered light intensity of Gsk(L308S) after adding 100 μM ppGpp compared to that of WT Gsk.
(I) Scheme showing the role of ppGpp binding and tetramerization in the inactivation of Gsk.
(J) Guanosine kinase activity of 50 nM WT and L308S Gsk in the presence of ppGpp at indicated concentrations.
(K) Specific guanosine kinase activity of ppGpp-bound WT and L308S as a function of enzyme concentration. Green line shows estimated percentage of dimeric Gsk based on the equilibrium: $2(Gsk)_2 = (Gsk)_4$. All reactions carried out in the presence of 1 mM ppGpp. Error bars show range of two separate reactions in (D-E), and S.D. of three separate reactions in (J-K).
See also Figure S3.

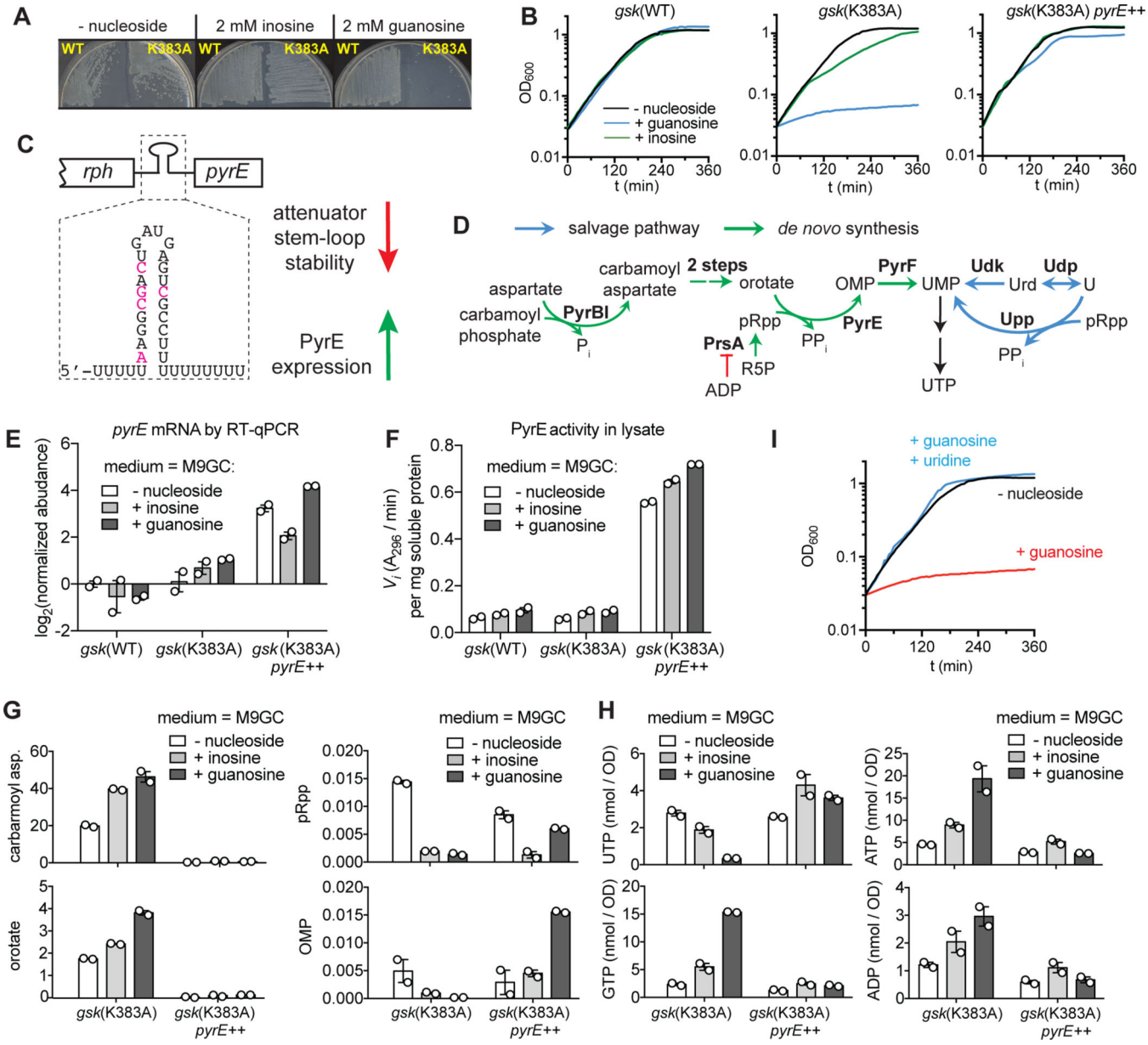

Figure 4. Feedback inhibition of Gsk maintains a balance between purine and pyrimidine nucleotide synthesis

(A) Growth of *gsk*(WT) and *gsk*(K383A) on M9GC agar plates containing indicated nucleosides.

(B) Growth curves of indicated strains after diluting stationary-phase cultures grown in M9GC into M9GC without or with indicated purine nucleosides.

(C) Scheme showing the attenuator element between the transcriptionally coupled *rph* and *pyrE* genes. Positions of suppressor mutations are highlighted in red. Also see Table S2 for a list of suppressor mutations identified on M9GC containing 2 mM guanosine.

(D) Pyrimidine synthesis (green) and salvage (blue) pathways.

(E-F) Quantification of (E) *pyrE* expression using RT-qPCR and (F) PyrE activity using an in-lysate orotate PRTase assay in steady-state cultures using indicated media.

(G-H) Quantification of (G) precursors/intermediates of UTP synthesis and (H) selected nucleotides in *gsk*(K383A) or *gsk*(K383A) *pyrE*++ cells in steady-state cultures using indicated media. In (G), y-axes are mass-spec peak area normalized to that of an internal standard, which is present at the same concentration in all samples. In (H), y-axes are absolute quantities, standardized using a working curve.

(I) Growth curves after diluting *gsk*(K383A) cells into M9GC medium supplemented with indicated purine/pyrimidine sources.

For panels A, B and I, one representative set of three separate cultures are shown. For panels E-H, error bars are range of two replicates taken from separate cell cultures.

See also Figure S4.

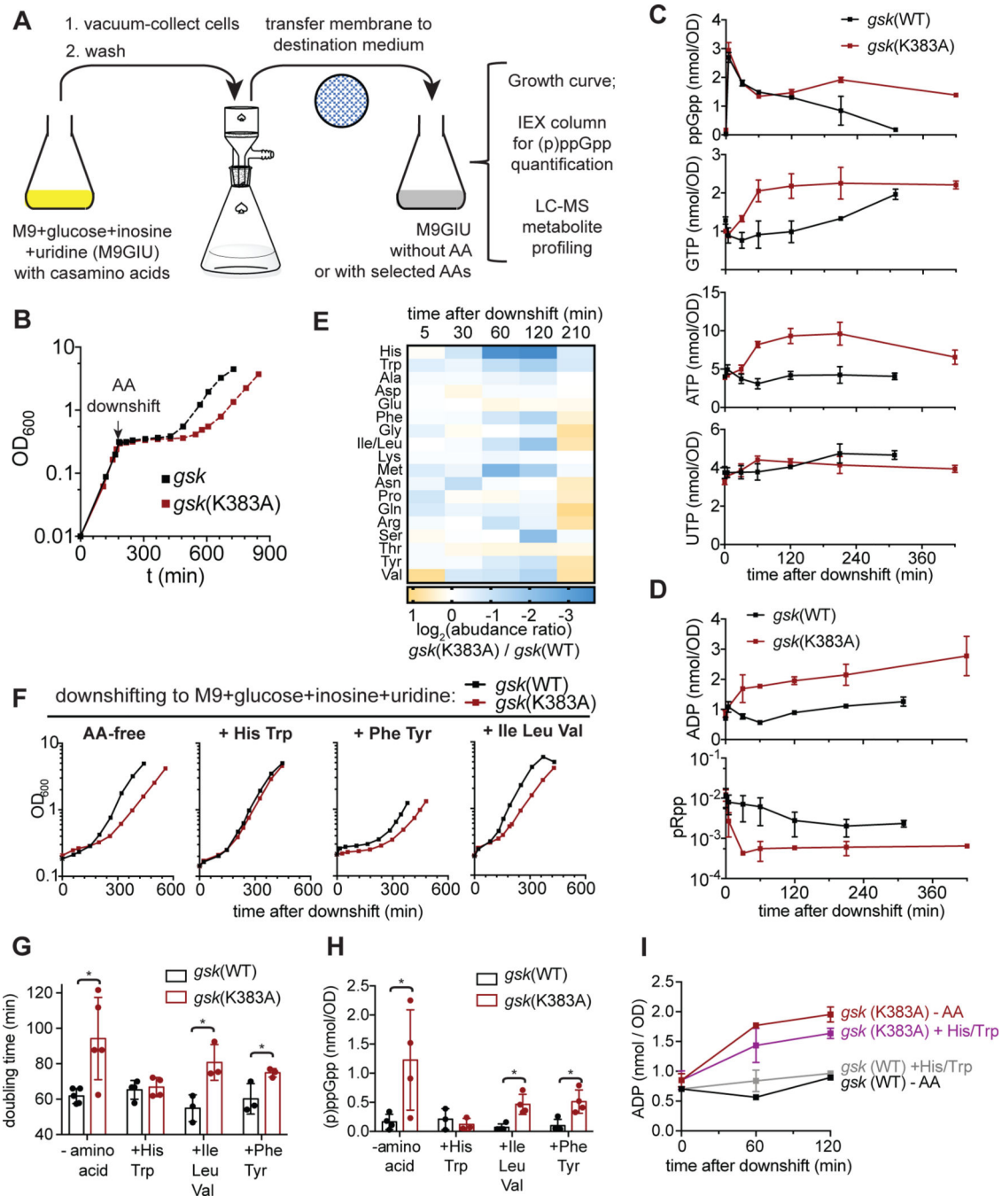

Figure 5. Inhibition of purine nucleotide synthesis after AA starvation preserves pRpp for the synthesis of histidine and tryptophan

(A) Scheme showing the work flow of the amino-acid downshift experiment.

(B) Growth curves of *gsk*(WT) and *gsk*(K383A) strains before (solid line) or after (dashed line) downshifting into amino-acid free M9GIU medium. One representative dataset from four independent downshift experiments is shown.

(C-D) Time course showing levels of indicated metabolites in *gsk*(WT) and *gsk*(K383A) strains before (t = 0) or after downshift into amino-acid free M9GIU medium. In (D), y-axis for pRpp is internal standard-normalized, mass-spec peak area.

(E) Heat map showing ratios of amino-acid levels in *gsk*(K383A) cells relative to *gsk*(WT) at indicated time points after downshifting into amino-acid free M9GIU medium. See also Figure S5C.

(F) Growth curves of *gsk*(WT) and *gsk*(K383A) strains after downshifting into M9GIU medium supplemented with indicated amino acids. The first data point of each curve is calculated assuming no loss of cells during transfer. One representative dataset from three or four independent cell cultures is shown for each condition.

(G-H) Generation time (G) and sum of ppGpp and pppGpp levels (H) of *gsk*(WT) and *gsk*(K383A) after recovery from downshift experiment in panel (E). See Methods section for details. Error bars indicate standard deviation. Asterisk indicates $p < 0.05$ (Student's *t*-test).

(I) Time course showing ADP levels in *gsk*(WT) and *gsk*(K383A) strains after downshifting into M9GIU medium that was AA-free or supplemented with histidine and tryptophan.

In (C), (D) and (I), error bars are range of two separate cell cultures.

See also Figure S5.

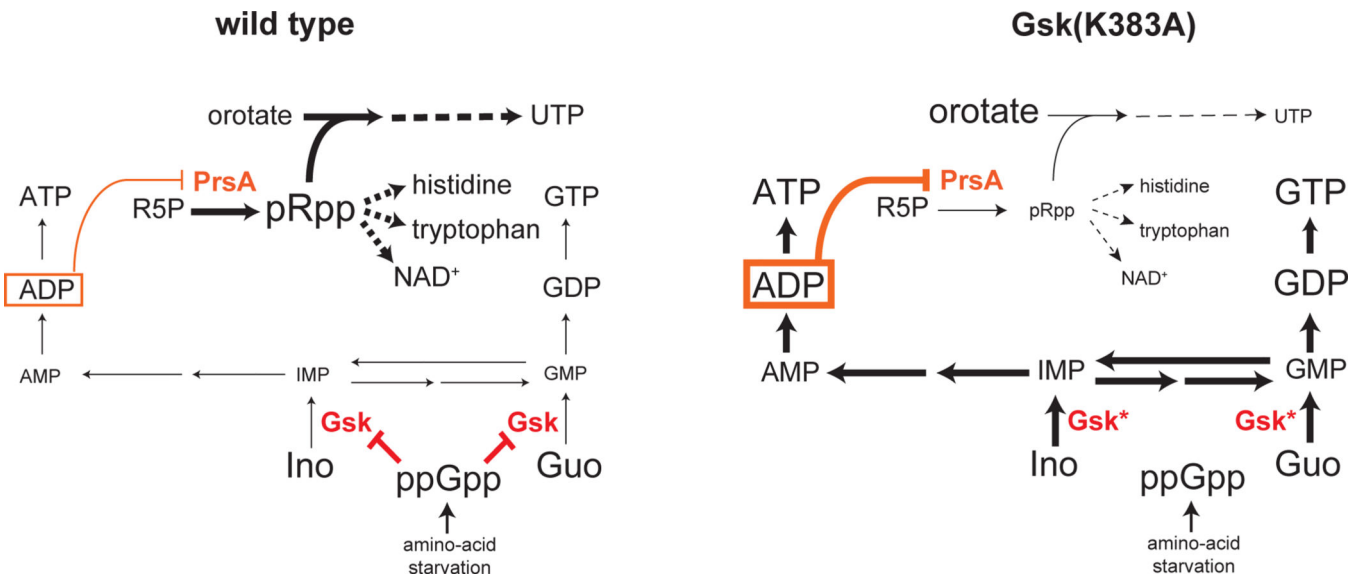

Figure 6. Metabolic rationale behind the inhibition of purine nucleotide synthesis by ppGpp

Comparison of purine nucleotide synthesis and related metabolic responses during amino-acid starvation in *E. coli* strains harboring wild-type *gsk* (left) and *gsk*(K383A) (right). Active and inactive pathways are in thick and thin arrows, respectively. Dashed arrow indicates multi-step processes. The critical regulatory inhibition of Gsk and PrsA by ppGpp and ADP are highlighted by red and orange flat-head arrows, respectively.

See also Figure S6.

Table 1.

Crystallographic data and refinement

	PDB 6VWO	**PDB 6VWP**
Resolution range (Å)	42.3 – 1.78 (1.85–1.78)	48.9 – 3.42 (3.54–3.42)
Space group	$P3_221$	$P3_121$
a,b,c (Å)	118.12, 118.12, 75.45	245.95, 245.95, 221.68
α,β,γ (°)	90,90,120	90,90,120
Unique reflections	55134	103858
Redundancy	16.6 (5.2)	16.7 (15.3)
Completeness (%)	95.0 (58.8)	99.4 (96.1)
Wilson B-factor	32.0	142.3
R-merge	0.083 (0.896)	0.117 (1.750)
R-pim	0.02 (0.381)	0.029 (0.461)
CC1/2	0.998 (0.732)	99.8 (0.699)
I/sigma I	22.06 (1.25)	17.69 (1.29)
R-work	0.181 (0.346)	0.200 (0.310)
R-free	0.205 (0.329)	0.242 (0.350)
RMSD bonds (Å)	0.006	0.005
RMSD angles (°)	0.87	0.75
Ramachandran favored (%)	98.15	95.73
Ramachandran outliers (%)	0.0	0.36
Clashscore	4.84	7.07
Average B-factor	42.0	146.0
# of atoms		
Protein (H included)	5888	50550
Ligands/ions (H included)	108	924
Water	204	0

Note: Values in ( ) for highest resolution bin